A multi-proxy investigation of mantle oxygen fugacity along the Reykjanes Ridge

Davide Novella[1,*,&], John Maclennan[1], Oliver Shorttle[1,2], Julie Prytulak[3,4], and Bramley J. Murton[5]

[1] Department of Earth Sciences, University of Cambridge, UK

[2] Institute of Astronomy, University of Cambridge, UK

[3] Department of Earth Sciences, Durham University, UK

[4] Department of Earth Science and Engineering, Imperial College London, UK

[5] National Oceanography Centre, University of Southampton, UK

* corresponding author: dn345@cam.ac.uk

[&] now at: Department of Earth and Environmental Sciences, Università degli Studi di Pavia, Italy; email: davide.novella@unipv.it

Abstract

Mantle oxygen fugacity (fO_2) governs the physico-chemical evolution of the Earth, however current estimates from commonly used basalt redox proxies are often in disagreement. In this study we compare three different potential basalt fO_2 proxies: Fe^{3+}/Fe_{tot}, V/Sc and V isotopes, determined on the same submarine lavas from a 700 km section of the Reykjanes Ridge, near Iceland. These samples provide a valuable test of the sensitivities of fO_2 proxies to basalt petrogenesis, as they formed at different melting conditions and from a mantle that towards Iceland exhibits increasing long-term enrichment of incompatible elements. New trace element data were determined for 63 basalts with known Fe^{3+}/Fe_{tot}. A subset of 19 lavas, covering the geographical spread of the ridge transect, was selected for vanadium isotope analyses.

Vanadium is a multi-valence element whose isotopic fractionation is theoretically susceptible to redox conditions. Yet, the $\delta^{51}V_{AA}$ composition of basaltic glasses along the Reykjanes Ridge covers only a narrow range ($\delta^{51}V_{AA}$= -1.09 to -0.86‰; 1SD= 0.02-0.09) and does not co-vary with fractionation-corrected Fe^{3+}/Fe_{tot} (0.134-0.151; 1SD= 0.005) or V/Sc (6.6-8.5; 1SD= 0.1-1.3) ratios. However, on a global scale, basaltic $\delta^{51}V_{AA}$ may be controlled by the extent of melting. The V/Sc compositions of primitive (MgO > 7.5 wt%) basalts show no systematic change along the entire length of the Reykjanes Ridge. Typical peridotite melting models in which source Fe^{3+}/Fe_{tot} is constant at 5% and that account for the increased mantle potential temperature nearer the plume center and the fO_2 dependent partitioning of V, can reproduce the V/Sc data. However, while these melting models predict that basalt Fe^{3+}/Fe_{tot} ratios should decrease with increasing mantle potential temperature towards Iceland, fractionation-corrected Fe^{3+}/Fe_{tot} of Reykjanes Ridge lavas remain nearly constant over the ridge length. This discrepancy is explained by source heterogeneity, where an oxidized mantle pyroxenite component contributes to melting with increasing proximity to Iceland.

Comparison of observed and modeled Fe^{3+}/Fe_{tot} indicate that source variation in fO_2 is present under the Reykjanes Ridge, with higher Fe^{3+}/Fe_{tot} closer to Iceland. This source variability in fO_2 cannot be resolved by V isotopes and redox-sensitive trace element ratios, which instead appear to record magmatic processes.

Keywords

mantle, oxygen fugacity, MORB, Fe^{3+}/Fe_{tot}, vanadium, isotopes

Introduction

Oxygen fugacity is an intensive thermodynamic property that dictates the oxidizing potential of a system (e.g., Frost, 1991). In the Earth's mantle, fO_2 controls phase relations, elemental distributions and magma genesis. As magmas rise, they retain an fO_2 inherited from their source, which controls the speciation and solubility of volatile elements and thereby the composition and volume of gasses they release to Earth's atmosphere (e.g., Frost and McCammon, 2008; Gaillard et al., 2011). Knowledge of mantle fO_2 is thus fundamental for interpretation and understanding of the physico-chemical processes that control the solid-Earth's interaction with the oceans and atmosphere.

One way to determine mantle fO_2 is through the study of mantle peridotites that are either tectonically emplaced into the crust or magmatically delivered to the surface as xenoliths. Oxygen fugacity can be quantitatively estimated from such rocks by application of a mineral oxybarometer, which quantifies the thermodynamics of redox reactions between mineral phases present (e.g., olivine-orthopyroxene-spinel, O'Neill & Wall, 1987). This approach has been used to demonstrate that in the continental lithosphere, fO_2 decreases with depth, from ±2 log units relative to the FMQ (fayalite-magnetite-quartz) buffer in the spinel peridotite field to -5 ΔFMQ in the deeper garnet peridotite field (Frost and McCammon, 2008 and references therein). However, the results from these studies are primarily representative of the cratonic lithospheric mantle, from which most xenoliths derive. In contrast to the cratons, the convecting mantle is poorly sampled by xenoliths, and its distinct chemical and thermal regime means that its fO_2 may not be well described by observations of cratonic xenoliths.

Basalts are more ubiquitous samples of the convecting mantle than xenoliths. Basalts that form in equilibrium with their mantle source and subsequently remain a closed system during ascent and surface emplacement will have an eruptive fO_2 related to their mantle fO_2 (Kress and Carmichael,

1991). A commonly used fO_2 proxy in basalts is their ferric iron content (Fe^{3+}/Fe_{tot}), which can be precisely determined by micro-scale techniques such as X-ray absorption near edge structure (XANES) spectroscopy (e.g., Berry et al., 2018; Cottrell et al., 2009). Through the determination of the ferric content of basalts, mantle fO_2 can be estimated following empirical thermodynamic calibrations and accounting for differentiation and degassing (e.g., Brounce et al., 2014, 2017; Helz et al., 2017; Kelley and Cottrell, 2012; Kress and Carmichael, 1991; Moussallam et al., 2014, 2016; Shorttle et al., 2015). Previous studies (see e.g., Brounce et al., 2014, 2015, 2017; Cottrell and Kelley, 2011, 2013; Hartley et al., 2017; Helz et al., 2017; Kelley and Cottrell, 2009; Moussallam et al., 2014, 2016; O'Neill et al., 2018; Shorttle et al., 2015) have indicated that the upper mantle is heterogeneous in terms of Fe^{3+}/Fe_{tot}, with more oxidized conditions found at arc settings ($fO_2 \geq$ FMQ+1) compared to mid ocean ridges (FMQ $\leq fO_2 \leq$ FMQ+0.5). Despite the prominence of using Fe^{3+}/Fe_{tot} in basalts as a tool for estimating convecting mantle fO_2, some work has also returned to the abyssal peridotite record to investigate its preservation of mantle fO_2. Birner et al. (2018) showed that peridotites and basalts from mid-ocean ridge settings have good agreement in their estimates of mantle fO_2, while new experimental work also supports this conclusion (Davis and Cottrell, 2018).

Importantly, different groups' XANES-derived estimates of Fe^{3+}/Fe_{tot} in mid ocean ridge basaltic glasses have recently shown offsets from each other (e.g., Berry et al., 2018; Zhang et al., 2018; see Results for a discussion of our data in this context). These differences reflect underlying decisions in the interpretation of the Mössbauer spectra of glasses, in particular whether at highly reducing conditions the spectra record the presence of ferric iron (Berry et al., 2018). As a result, the Berry et al. (2018) XANES calibration, for a given sample, estimates lower ferric iron contents than the Zhang et al. (2018) calibration. Debate continues around the correct choice of calibration (Berry et al., 2018; Cottrell et al., 2009; Zhang et al., 2018; see Results). However, what is more significant for this study is simply the thermodynamic basis for relating ferric iron abundances to fO_2 – i.e., that

changes in Fe^{3+}/Fe_{tot} within a sample suite of relatively constant major element chemistry relate to variation in fO_2, something which the question of XANES calibration does not directly affect.

Another potential tracer of mantle fO_2 in basalts is their V/Sc ratio, which uses the oxygen fugacity dependence of the partition coefficients of V between minerals and melts $D_v^{min/melt}$ (e.g., Canil, 1997, 1999). Vanadium and Sc are mildly incompatible trace elements that behave similarly during melting, but while Sc is homovalent in igneous systems (Sc^{3+}), V is multivalent (V^{2+}, V^{3+}, V^{4+}, V^{5+}). This creates an fO_2 dependence to V partitioning during melting as the different valence states of V have different partition coefficients: $D_v^{min/melt}$ decreases with increasing fO_2 whereas $D_{Sc}^{min/melt}$ remains constant (e.g., Canil, 1997, 1999; Mallmann & O'Neill, 2009), resulting in higher V/Sc in basalts that form at more oxidizing conditions (Lee et al., 2003, 2005; Li and Lee, 2004). Employing V/Sc to estimate mantle fO_2 requires a correction for fractional crystallization, and therefore alternative ratios, such as V/Yb, have been proposed (Laubier et al., 2014). Importantly, in contrast to Fe^{3+}/Fe_{tot}, V/Sc ratios of MORBs and arc basalts have similar values, an observation which has been used to argue that the convecting mantle, whether beneath arcs or ridges, has a relatively uniform fO_2 at ~FMQ-0.5 (Lee et al., 2005). Thus, current estimates of mantle fO_2 determined by these two commonly used proxies are in significant disagreement.

Mantle fO_2 might also be investigated by studying the stable isotopic composition of multivalent transition metals in basaltic magmas (see review in Teng et al., 2017). This is because stable isotope fractionation depends on valence state and coordination number. Vanadium is an element of interest in this respect because of its multiple valence states. Also, V isotopic compositions are not disturbed by secondary processes such as weathering or hydrothermal alteration (Prytulak et al., 2013; Wu et al., 2018), which can affect other isotopic systems (e.g., Fe; Rouxel et al., 2003). However, the effects of fO_2, magmatic differentiation, partial melting and source heterogeneity need

156 to be understood before applying V isotopes as a mantle fO_2 proxy (Prytulak et al., 2013, 2017;
157 Sossi et al., 2018; Wu et al., 2018).
158
159 In this study, a suite of mantle-derived basalts from a ~700 km long segment of the Reykjanes
160 Ridge near Iceland was selected to investigate the behaviour of Fe^{3+}/Fe_{tot}, V/Sc and V isotopes to
161 assess their co-variation and suitability as fO_2 proxies. Fe^{3+}/Fe_{tot} data from Shorttle et al. (2015)
162 were recalibrated using the most recent values for the XANES reference standards (Zhang et al.,
163 2018) and combined with new trace element concentrations on 63 basalt glasses and V isotopic
164 compositions on a representative subset of 19 lavas (Fig. 1). The Reykjanes Ridge samples are well
165 characterized in terms of major and minor element concentration and display systematic variations
166 of trace element ratios and radiogenic isotopic composition with distance from Iceland (e.g., Murton
167 et al., 2002; Schilling, 1973). Pyroxenitic sources are inferred to be an important component feeding
168 magmatism on subaerial Iceland (e.g., Stapafell on the Reykjanes Peninsula where the ridge comes
169 ashore; Fig. 1), and may also extend down the ridge and affect the genesis of Reykjanes Ridge
170 basalts (Shorttle and Maclennan, 2011; Shorttle et al., 2010). In addition, the crustal thickness along
171 the Reykjanes Ridge is well determined (e.g., Jones et al., 2014 and references therein) enabling
172 precise constraints on mantle melting conditions and potential temperature (T_p), which gradually
173 rises by 60 °C towards Iceland (see e.g., Matthews et al., 2016). The degree of basalt differentiation
174 also increases along-ridge, as the crust thickens. Thus, the Reykjanes Ridge is an excellent locality
175 to evaluate the co-variation of potential fO_2 proxies during mantle melting and the influence of both
176 low-pressure differentiation and lithological heterogeneity. In addition to comparison of potential
177 proxies, thermodynamic melting models were employed to further disentangle the interplay
178 between source fO_2, melting, and lithological heterogeneity.
179

180 **2. Methods**

181 **2.1 Vanadium isotopes**

Chemical isolation of vanadium was conducted in the MAGIC laboratories at the Department of Earth Sciences and Engineering, Imperial College London. Clean glass shards without visible minerals, air/fluid inclusions or weathering features were hand-picked under an optical microscope and ground in an agate mortar to obtain a homogeneous, fine powder. Approximately 30 mg of each sample was weighed to provide between 5 and 10 μg of total V. The samples were digested in a 2:1 mixture of 28M HF:15 M HNO_3 at 160 °C for at least 1 day. The samples were then evaporated and re-dissolved in 15M HNO_3. This step was repeated 3-5 times in order to ensure the complete destruction of the fluorides that form during digestion. The dissolved basalts were processed through ion exchange chromatography following the protocol of Nielsen et al. (2011). This technique describes a 7-column procedure that allows for complete separation of V from the matrix and, in particular, quantitative removal of Cr and Ti that can cause isobaric interferences on the minor isotope ^{50}V.

Vanadium isotopic compositions were measured with a Nu Plasma II multi collector inductively coupled plasma mass spectrometer (MC-ICPMS) at Imperial College London following the procedure outlined in Hopkins et al. (2019). Vanadium isotopic compositions were determined by standard-sample bracketing, and are reported as permil variations relative to the Alpha Aesar (AA) V standard solution (Nielsen et al., 2011) using the standard delta notation:

$$\delta^{51}V_{AA} = 1000 \times [(^{51}V/^{50}V_{sample} / {}^{51}V/^{50}V_{AA}) - 1].$$

A secondary standard solution from BDH chemicals and the NIST 3165 solution were measured during each session to monitor instrument stability. Samples and standards were diluted to a V concentration of 600 ppb. Total procedural blanks were insignificant (< 2ng) compared to the amount of V processed. Analysis of USGS reference materials (BIR-1a, BCR-2 and AGV-2) and the BDH and NIST 3165 solution standards are in agreement with published literature (Table S1).

208

209 **2.2 Laser ablation inductively coupled plasma mass spectrometry**

210 Trace and rare earth element (REE) concentrations were measured by laser ablation inductively
211 coupled plasma mass spectrometry (LA-ICPMS) at the Department of Earth Sciences, the
212 University of Cambridge. This analytical setup combines a NWR193 excimer laser ablation systems
213 with a Perkin Elmer NexION 350D ICP mass spectrometer. The list of the trace elements analyzed
214 and their concentrations are reported in Table S2. Measurements were conducted on 63 polished
215 glasses that were previously analyzed by XANES to determine Fe^{3+}/Fe_{tot} (Shorttle et al., 2015). Spot
216 analyses of 100 μm diameter were conducted on clean portions of the glasses, avoiding potential
217 sources of contamination such as cracks or inclusions, using a laser power of 8 J/cm^2 and 10 Hz
218 repetition rate. These ablating conditions were optimized after testing international reference glass
219 standards NIST-612, BCR-2G, BIR-1G and ML3B-G and comparing with the preferred values from
220 the GEOREM database (available at http://georem.mpch-mainz.gwdg.de). The data were collected
221 by the ICP-MS using 1 sweep per reading, 50 readings and 1 replicate conditions. ICP-MS dwell
222 time varied for the different elements and it was typically between 10-20 ms for most trace
223 elements, but this value was increased up to 60 ms for some low concentrations REE. The Glitter
224 Software (GEMOC, Australia) was used to process raw data (signal intensity vs time), which allows
225 to the user to select backgrounds and signals and precisely calculate sample concentrations. The
226 SiO_2 content of the glasses, previously determined by electron microprobe analyses (Shorttle et al.,
227 2015), was used as internal standard for the normalization of trace element signals. BCR-2G was
228 chosen as an external standard as it provided, overall, better precision (RSD% generally <10%,
229 1SD) and accuracy (average percent error within ±15%) compared to other standards. These values
230 of precision and accuracy were calculated considering all individual analyses collected on a
231 particular standard at the beginning, middle and end of the session.

232

233 **2.3 Modelling rationale**

Two types of mantle melting scenarios were explored to reproduce the Fe^{3+}/Fe_{tot} and trace element variation along the Reykjanes Ridge. The first approach was adopted to simulate adiabatic melting of ambient mantle peridotite. The second was conducted to investigate the melting behavior of pyroxenite and in particular the formation of enriched lavas, using the Stapafell eruption from subaerial Iceland as an endmember (Fig. 1). Thermodynamic modelling was performed with the pMELTS software operated through the alphaMELTS frontend (Ghiorso et al., 2002; Smith and Asimow, 2005). pMELTS was used to predict the equilibrium phase assemblage of a mantle composition at given conditions (P, T and fO_2). The chemical composition of the modelled instantaneous melts was calculated from the phase equilibria and melting reactions. A general description of the modelling rationale is provided below, while more details are reported in Table S3.

(1) DMM melting: Depleted MORB mantle (DMM) major element composition from Workman and Hart (2005) was used as a starting composition, with varying initial Fe^{3+}/Fe_{tot} ratios (4-6%) calculated maintaining constant total FeO_T. These Fe^{3+} contents are chosen such that the model produces melts with a range of Fe^{3+}/Fe_{tot} close to that observed. A mantle Fe^{3+}/Fe_{tot} of 4-6% is slightly higher than values predicted based on mantle xenolith studies (Fe^{3+}/Fe_{tot} = 2%; e.g., Canil and O'Neill, 1996). There may be two reasons for this: (1) model-based effects, whereby the treatment of ferric iron in pMELTS is not accurately capturing its behavior in natural systems (e.g., the lack of ferric iron in garnet in pMELTS, despite its presence in garnet solid solution as andradite); (2) the possibility that cratonic xenoliths underestimate convecting mantle fO_2 values. However, this study is focused on the *relative* changes in Fe^{3+}/Fe_{tot} rather than absolute values, so our choice of mantle Fe^{3+}/Fe_{tot} is less important than how it translates to basalt Fe^{3+}/Fe_{tot}, given changing conditions of melt generation along ridge.

Model simulations of decompression fractional melting were conducted for changing mantle potential temperatures along the Reykjanes Ridge to account for the influence of the Icelandic plume on the sub-ridge thermal structure. Potential temperatures increasing from 1404 °C at ~1100 km to 1468 °C at ~400 km (Table S2), were constrained by matching the melt thickness produced by decompression melting models of DMM with the crustal thickness reported by seismological surveys (e.g., Jones et al., 2014 and references therein). Mantle fO_2 was not imposed in the models and was calculated using the Fe^{3+}/Fe_{tot} ratio of the melts (Kress and Carmichael, 1991) with pMELTS considering that Fe^{3+} is not incorporated in olivine and garnet. It is recognized, however, that in pMELTS fO_2 can be also calculated based on solid phase equilibria (Asimow and Ghiorso, 1998) and that this method provides systematically less oxidized values compared with the above calibration. The fO_2 determined with the Kress and Carmichael (1991) calibration was used here for consistency with data from natural samples.

Adiabatic decompression models were used to calculate the major element compositions (SiO_2-TiO_2-Al_2O_3-Fe_2O_3-Cr_2O_3-FeO-MgO-CaO-NaO) of progressive aggregate melts in a 2D triangular melting region. Even though pMELTS allows for the direct calculation of trace element concentrations, their behavior here was treated separately so that the effect of fO_2 on the distribution of V between minerals and melts could be incorporated (e.g., Canil, 1997). Partition coefficients of V were calculated following the parameterization of Mallmann and O'Neill (2009, 2013) while those for selected trace elements (Sc, Ba, La, Nb, Zr, K) used the values of M^{c}Kenzie & O'Nions (1991, 1995) and Mallmann & O'Neill (2009). These particular elements were chosen to monitor the behavior of trace element ratios in the models and track enrichment along the ridge (see discussion). The trace element compositions of the melts were calculated assuming a depleted mantle source of Salters & Stracke (2004), which provide concentrations for all elements of interest, and the phase compositions, modal abundances and P, T and fO_2 from the pMELTS calculations.

285 *(2) Pyroxenite melting*: Modelling the composition of melts produced by melting of a bi-lithological
286 mantle, containing a mechanical mixture of peridotite and pyroxenite, is challenging due to the
287 variety of melt-rock reactions that can occur. pMELTS does not currently allow for direct
288 calculation of melting of a bi-lithological mantle and instead a multi-step approach, where the
289 lithologies are modelled separately and combined, needs to be followed (Rudge et al., 2013). A
290 further complexity for modelling pyroxenite melting is that its low solidus temperature means that
291 melting begins above 4 GPa at the potential temperatures investigated here, which is outside the
292 calibrated pressure range of pMELTS. We therefore made a first-order investigation of pyroxenite's
293 effect on the composition of aggregate melts, discounting the full chemical and physical complexity
294 a more complete model would need to incorporate. Only an initial stage of isobaric melting of
295 mantle pyroxenite was modelled here, as described by Rudge et al. (2013). This approximates
296 adiabatic decompression melting by instead conducting isobaric melting calculations in the
297 calibrated pressure range of pMELTS. Assuming that the melt productivity (i.e., dF/dP) is known
298 for the pyroxenite, the isobaric calculations can be approximately related to a decompression
299 interval. Low-degree model melts are finally compared to Stapafell lavas in order to assess trace
300 element enrichment of Reykjanes Ridge basalts.
301
302 The pyroxenite chosen for modelling was KG1 from Kogiso et al. (1998), which compositionally
303 corresponds to a 1:1 peridotite:basalt mixture. The Fe^{3+}/Fe_{tot} of this lithology was set at 16%
304 assuming KG1 represents a peridotite with 5% Fe^{3+}/Fe_{tot} (DMM models) mixed with a Proterozoic
305 basalt with 27% Fe^{3+}/Fe_{tot} ratio (e.g., Stolper and Keller, 2018). Proterozoic basalts can be
306 envisaged as remnant subducted slab in the mantle that were oxidized during seafloor weathering
307 (Stolper and Keller, 2018). The trace element concentrations of KG1 were also calculated by
308 mixing peridotite from Salters and Stracke (2004) with recycled oceanic crust from Stracke et al.
309 (2003). If not reported in Stracke et al. (2003), the concentration of certain elements of the recycled
310 oceanic crust were calculated using the N-MORB mean of Gale et al. (2013) and the

supercomposite altered MORB composition from Bach et al. (2003). Concentrations of elements with high mobility were recalculated using the dehydration model of Stracke et al. (2003). Model calculations were performed for a pressure of 3 GPa, which corresponds to the onset of melt extraction of DMM source at the highest T_p (approaching Iceland). Partition coefficients varying with P, T and composition were used and no fixed fO_2 was imposed (Table S3).

3. Results

3.1 Vanadium isotopic compositions

The V isotopic composition of the Reykjanes Ridge basalts ranges between -1.09 and -0.86‰ (Table S2), and extends towards lighter values from the global average for MORB (-0.84‰ ± 0.10 2SD, n= 22; Wu et al., 2018). No systematic variation is observed along the 700 km transect of the ridge (Fig. 2), with Fe^{3+}/Fe_{tot} (Fig. 3a) or with V/Sc ratio (Fig. 3b). The average of all Reykjanes Ridge basalts is -0.97‰ ±0.17 2SD (n=19) and overlaps with the MORB average value of Wu et al. (2018). In detail, the Reykjanes Ridge basalts are the light isotope end-member in the positive global correlation between Na_8 and $\delta^{51}V$ determined by Wu et al. (2018) (Fig. 4).

3.2 Trace elements

Trace element concentrations are summarized in Table S2. The V/Sc ratios range between 6.5 and 10 and are displayed in Fig. 5 as a function of distance from Iceland and MgO content. The V/Sc ratio increases approaching Iceland, however, this signal negatively correlates with MgO contents indicating the strong effect of fractional crystallization (e.g., Li and Lee, 2004). Specifically, Fig. 6 shows that samples with V/Sc > 8.5 have CaO <11.9 wt% and MgO <7.3 wt%, demonstrating that low pressure clinopyroxene fractionation is responsible for fractionating V from Sc (Fig. S1). Primitive Reykjanes Ridge basalts with MgO >7.5 wt%, however, are not affected by clinopyroxene crystallization (Fig. 6 and S1) and show no systematic changes in V/Sc along the

ridge ranging between 6.5 and 8.5, in agreement with the average MORB value of 6.7 (Lee et al., 2005).

The incompatible trace element ratio Nb/Zr increases from 0.02 at 1100 km to 0.11 at 400 km distance along the Reykjanes Ridge (Table S2), which has been interpreted to reflect a greater proportion of plume-fed enriched material closer to Iceland (e.g., Murton et al., 2002; Schilling, 1973; Shorttle and Maclennan, 2011). Short length scale heterogeneity along the Reykjanes Ridge is also shown by the chemically anomalous seamount 14D, which has Nb/Zr =0.08 at ~1100 km from the Icelandic plume center (Table S2). This is 4 times above local background values and closer to the average crustal composition of subaerial Iceland (Shorttle et al., 2015).

3.3 Fe^{3+}/Fe_{tot} ratios revisited from Shorttle et al. (2015)

Shorttle et al. (2015) performed micro XANES on the same Reykjanes Ridge basalts that were investigated in this study. Their work determined their Fe^{3+}/Fe_{tot} ratios using the standards from the Smithsonian NMNH (catalog #117393) described in Cottrell et al. (2009). By evaluating time-resolved XANES spectra, Shorttle et al. (2015) ruled out beam damage causing oxidation effects.

However, since the work of Shorttle et al. (2015), cryogenic Mössbauer analyses were used to re-determine the Fe^{3+}/Fe_{tot} ratios of the standards developed by Cottrell et al. (2009), with the original Mössbauer work having been performed at room temperature (Zhang et al., 2018). Zhang et al.'s (2018) re-analysis of the standards provides lower Fe^{3+}/Fe_{tot} estimates, with their work suggesting a differential temperature-dependent response of the Fe^{3+} and Fe^{2+} Mössbauer doublets that has compromised previous room-temperature Mössbauer work. As such, when the raw XANES spectra of Shorttle et al. (2015) were reprocessed in this study using the Zhang et al. (2018) calibration, their Fe^{3+}/Fe_{tot} decreased (Table S2). Additionally, a more conservative measure of how to relate spectral shape to Fe^{3+}/Fe_{tot} was used in the quantifying of the XANES spectra here than had

originally been used by Shorttle et al. (2015) (who employed a principal component regression of the entire pre-edge region). The peak area ratio was used in this study to form a calibration following Zhang et al. (2016), as it showed the least compositional sensitivity. Although there is limited major element variability in this sample suite, what variation there is co-varies with distance along ridge (via igneous differentiation), so the peak area ratio approach minimizes that chance that this is aliased into Fe^{3+}/Fe_{tot} estimates.

Berry et al. (2018) and O'Neill et al. (2018) have recently argued for a different interpretation of the Mössbauer spectra underpinning the Fe^{3+}/Fe_{tot} of the XANES standards of Cottrell et al. (2009). This interpretation would suggest that the recalibrated Shorttle et al. (2015) Fe^{3+}/Fe_{tot} should be systematically lowered by a further 2-3% (absolute). However, the differences between the Berry et al. (2018) and the Zhang et al. (2018) calibrations do not translate to significant differences in inferred fO_2, because the Berry et al. (2018) calibration has been linked to a re-parameterization of how basalt Fe^{3+}/Fe_{tot} is related to fO_2 (O'Neill et al., 2018). The result is that either using Zhang et al. (2018) with Kress and Carmichael (1991), or Berry et al. (2018) with O'Neill et al. (2018), the inferred mantle fO_2 from basalts is nearly constant at ~FMQ.

Importantly, it is emphasized that this study is focused on understanding *relative* fO_2 variation along the Reykjanes Ridge and how this is reflected in changes in the various fO_2 proxies. As such, further comments on the cause of absolute discrepancies in Mössbauer-based XANES calibrations are not developed.

The recalibrated Fe^{3+}/Fe_{tot} data of the Reykjanes Ridge basalts are reported in Table S2 and displayed in Fig. 7a. The raw Fe^{3+}/Fe_{tot} ratios range between 0.141 and 0.162, which is lower than the range of 0.155 to 0.175 previously reported by Shorttle et al. (2015). The highest values are observed in the seamount samples 17D1 (0.158) and 14D (0.162) that are recognized as local

heterogeneities (Murton et al., 2002; Shorttle et al., 2015), with the rest of the Reykjanes Ridge basalts reaching a maximum Fe^{3+}/Fe_{tot} ratio of 0.157. An error on Fe^{3+}/Fe_{tot} of 0.5% (absolute) is estimated from the long term reproducibility of the standards used during the XANES sessions of Shorttle et al. (2015).

The effect of crystallization on the ferric iron content of the lavas (e.g., Cottrell and Kelley, 2011) can be seen in Fig. 7a, where more evolved basalts with lower MgO have higher Fe^{3+}/Fe_{tot} ratios. The raw data calculated here were corrected for crystallization using the two-stage approach of Shorttle et al. (2015), which combines a an empirical correction to 8 wt% MgO with olivine addition to 10 wt% MgO. Results are shown in Fig. 7b, where Fe^{3+}/Fe_{tot} ratios corrected to 10 wt% MgO (MgO_{10}) are now shifted to lower values between 0.131 and 0.151. These Fe^{3+}/Fe_{tot} ratios are in agreement with recent MORB averages (0.143) determined by Zhang et al. (2018) using XANES. The fractionation-corrected Fe^{3+}/Fe_{tot} (Fig. 7b) are used in the discussion that follows and for comparison with model results. Oxygen fugacities calculated using the Fe^{3+}/Fe_{tot} MgO_{10} ratios and the calibration of Kress and Carmichael (1991) at 2 kbar range between QFM+0.06 to QFM-0.32 (Fig. 7c). However, it is remarked again that rather than absolute Fe^{3+}/Fe_{tot} ratios, this study focuses on the differences between natural and modelled observations.

3.4 Melting models

Given the restricted range of $\delta^{51}V$, the lack of systematic co-variation with other chemical parameters (Fig. 2, 3) and the scarcity of isotopic mineral-melt fractionation factors, modelling focused on reproducing the Fe^{3+}/Fe_{tot}, V/Sc and Nb/Zr ratio of the melts along the Reykjanes Ridge (Fig. 8, Table S4).

In all DMM melting models, garnet is the first phase to disappear from the mantle residue during decompression melting, followed by clinopyroxene. For example, for the DMM composition with

5% bulk Fe^{3+}/Fe_{tot} and at the lowest T_p investigated (1404 °C), garnet disappears at approximately 2.2 GPa and clinopyroxene at 0.8 GPa. The same behavior is observed at higher T_p, with phases being consumed in the solid assemblage at slightly higher pressures. At T_p = 1404 °C, melt is first produced at approximately 1.9 GPa and is first extracted from the peridotite at slightly shallower depths, 1.8 GPa, when minimum porosity values of 0.5% (vol.) are reached (see constrains from e.g., Sims et al., 1999). At the highest T_p investigated (1468 °C), melts begin to form at higher pressure, 3.4 GPa, and begin separating from the residue at 3.0 GPa. Aggregate melt calculations stop at the base of the crust (determined by pressure of the overlying melt-derived crust) at a particular T_p along the Reykjanes Ridge. These pressures at the base of the crust range from 0.21 GPa in the south to 0.32 GPa at the northern most section of the ridge, corresponding to crustal thicknesses of ~7 and 11 km, respectively (assuming 2900 kg/m^3 as an average crustal density). Over the 1404 °C to 1468 °C T_p range considered, maximum extents of melting (F) increase from 25% to 29%.

Modelled Fe^{3+}/Fe_{tot} ratios of the aggregate melts decrease towards Iceland as higher potential temperatures are encountered (Fig. 8a; Table S4). Depending on source Fe^{3+}/Fe_{tot}, decreases of between 0.02 and 0.03 Fe^{3+}/Fe_{tot} in the modelled aggregate melt compositions are observed as T_p increases by 64 °C (i.e., from 1404 °C to 1468 °C), with associated decrease in melt absolute fO_2 between 0.78 and 0.83. This result is consistent with the findings of Gaetani (2016), who also showed that higher mantle temperatures produce more reduced aggregate melts. The calculated V/Sc ratio of partial melts produced also reflects changes in fO_2 (Fig. 8b), indicating an increased average Dv/D_{Sc} during melting towards Iceland (Table S4). However, V/Sc only exhibits a low amplitude response to these changing melting conditions, varying by only 0.7-0.9 at a given Fe^{3+}/Fe_{tot} source concentration over the investigated range of T_p (Fig. 8b). As expected for highly incompatible and fO_2 insensitive elements, the calculated Nb/Zr ratio in the melts are near constant at ~0.03 along the Reykjanes Ridge (Fig. 8c), regardless of the initial bulk Fe^{3+}/Fe_{tot} (Table S4).

The pyroxenite modelling focused on calculating Fe^{3+}/Fe_{tot} and trace element ratios, where disparities between the melt concentrations from the DMM models and the Reykjanes Ridge basalts are observed at distances < 700 km to Iceland (Fig. 8a, c). The low-degree (F%= 0.2 to ~20%) melt compositions formed in the KG1 pyroxenite melting models are reported in Table S5. In the isobaric melting model at 3 GPa, pyroxenite starts melting at 1384 °C and melts are extracted from the solid assemblage (consisting of olivine + garnet + clinopyroxene + spinel) at 1394 °C, when the porosity is higher than 0.5% (vol.). With increasing temperature, orthopyroxene becomes a stable phase in the solid assemblage with abundances increasing as melting proceeds. This is contrary to clinopyroxene abundances, which decrease as it is consumed on melting. Spinel is the least abundant phase in the solid assemblage and its abundance also slightly decreases with increasing temperature. As a result of these melting reactions, the liquid's Fe^{3+}/Fe_{tot} increases with increasing extent of melting as clinopyroxene (the dominant phase in the solid assemblage and major host of Fe^{3+}) and spinel (another reservoir of Fe^{3+} in its magnetite component) are progressively consumed. Trace element ratios used to indicate enrichment towards Iceland (e.g., Nb/Zr, La/Yb) are high in these melts (Table S5). For example, the calculated Nb/Zr ratio of the isobaric melts produced by melting KG1 pyroxenite ranges between 0.12 and 0.04 at melt fractions 0.2 and 20%, respectively, which are higher than the ratios produced in the DMM models at any T_p (Table S4).

Discussion

4.1 Vanadium isotopes as an fO_2 proxy

The $\delta^{51}V$ measured thus far in basaltic lavas with >4 wt% MgO have limited variation (Prytulak et al., 2013, 2017; Wu et al., 2018). However, an increase of ~2‰ in $\delta^{51}V$ towards heavier $\delta^{51}V$ values during progressive closed-system fractional crystallization of genetically related magmas has been ascribed mainly to the crystallization of isotopically light iron oxides (Prytulak et al., 2017; Sossi et al., 2018). The Reykjanes Ridge basalts investigated in this study all have MgO contents >6.3 wt%

(Shorttle et al., 2015), and thus fractional crystallization is not expected to influence their V isotopic signatures. The Reykjanes Ridge basalts display coherent and significant variation in trace element (e.g. Nb/Zr) and radiogenic isotopic compositions (e.g., $^{87}Sr/^{86}Sr$ and $^{143}Nd/^{144}Nd$; Murton et al., 2002). Increasing enrichment along the Reykjanes Ridge on approach to Iceland is commonly interpreted as the influence of the Icelandic mantle plume (e.g., Murton et al., 2002; Schilling, 1973). Murton et al. (2002) explained the geochemical variations of the Reykjanes Ridge basalts by mixing of six differently enriched mantle components. Thus, the data presented here suggest that V isotopes are not sensitive to the chemical heterogeneities in the mantle source below the Reykjanes Ridge documented by trace element and radiogenic isotope systems. This point is emphasized by the unremarkable V isotopic composition of sample 14D of $\delta^{51}V = -1.09$ (Fig. 2), which in terms of its trace elements and radiogenic isotopes clearly samples a local mantle compositional heterogeneity.

Wu et al. (2018) recently proposed that V isotope fractionation may be sensitive to the extent of melting by demonstrating a positive correlation between $\delta^{51}V$ and Na_8, an indicator of the degree of melting (Klein and Langmuir, 1987). The Reykjanes Ridge basalts have Na_8 between 1.83 and 2.19, and are displaced to isotopically lighter values compared with higher Na_8 MORB (Fig. 4). The Reykjanes Ridge basalts follow the general trend established by Wu et al. (2018), supporting the notion that the extent of melting may influence the V isotopic composition of MORBs on a global scale.

Importantly, the V isotopic compositions of the Reykjanes Ridge basalts do not correlate with Fe^{3+}/Fe_{tot} or V/Sc (Fig. 3). This observation indicates that V isotopes of primitive basalts are not sensitive to an fO_2 difference of ~0.3 log unit along the Reykjanes Ridge. However, primitive samples not affected by fractional crystallization and equilibrated at more extreme fO_2 conditions,

need to be analyzed to further assess the sensitivity of V isotopes to redox conditions for their use as an fO_2 sensor.

4.2 V/Sc as an fO_2 proxy

The V/Sc ratio of the partial melts calculated by pMELTS are compared to the Reykjanes Ridge compositions in Fig. 8b. The $D^{peridotite/melt}$ of trace elements is calculated based on $D^{min/melt}$ and the modal abundances of the minerals in the solid residue, which change as a function of T_p and P during decompression. The average V partition coefficients increase towards Iceland, where higher potential temperatures are met and resultingly lower fO_2's are calculated; the average Sc partition coefficient only slightly increases towards Iceland due to the deeper onset of melting, meaning that garnet is residual in the phase assemblage during proportionally more of the melting interval, and garnet has the highest D_{Sc} (Table S4). The net effect of these processes is for D_V/D_{Sc} to increase towards Iceland, resulting in the gently decreasing V/Sc ratio observed in the accumulated partial melts generated by pMELTS (Fig. 8b). The melting model of DMM with initial 5% Fe^{3+}/Fe_{tot} reproduces, within error, the V/Sc ratios of the primitive (>7.5 wt% MgO) Reykjanes Ridge basalts along the entire extent of the ridge between 1100 and 400 km (Fig. 8b). The V/Sc of primitive basalts translates into fO_2's ranging between ΔFMQ = 0 to -0.5 following the model of Lee et al. (2005). These fO_2 values are consistent with those calculated from the Fe^{3+}/Fe_{tot} (Fig. 7c). However, interpretations of mantle fO_2 values determined by V/Sc proxy are model-dependent, as the V/Sc concentration of basalts depends on both $D_v^{min/melt}$ and $D_{Sc}^{min/melt}$, the source concentrations and the fO_2 conditions. For example, Prytulak et al. (2017) used batch melting calculations to illustrate that a less oxidized, fertile mantle and a more oxidized, depleted mantle, with respectively higher and lower $D_v^{pdt/melt}$, can produce similar V/Sc ratios in MORB and arc lavas, highlighting the limitations of V/Sc as a direct redox proxy (see also Bucholz and Kelemen (2019) for this discussion in an arc context).

4.3 Fe^{3+}/Fe_{tot} as an fO_2 proxy

The ferric iron content of partial melts formed during adiabatic decompression of mantle peridotite reflects both source Fe^{3+}/Fe_{tot} and T_p. At a fixed source Fe^{3+}/Fe_{tot}, the upwelling mantle peridotite crosses fO_2 isopleths that become slightly more oxidized through the spinel stability field (Gaetani, 2016). Instantaneous melts may therefore become more oxidized as decompression proceeds. However, aggregate melts are also sensitive to the onset of melting, and when melting begins in the garnet field, at Tp > 1447 °C, the Fe^{3+}/Fe_{tot} of the aggregate melts decreases until garnet is exhausted from the solid assemblage. The net effect is that the Fe^{3+}/Fe_{tot} of aggregate melts decreases with increasing potential temperatures (Gaetani, 2016), as observed in the model runs as Iceland is approached (Fig. 8a).

Melting models of DMM composition with 5% initial Fe^{3+}/Fe_{tot} reproduce the Reykjanes Ridge basalt compositions between ~700 and 1100 km from the plume, in agreement with the V/Sc data (Fig. 8a-b). The highest Fe^{3+}/Fe_{tot} ratios of seamounts 14D and 17D, which formed from particularly enriched sources far from Iceland (Murton et al., 2002), are in agreement with the model, given the 0.01 2SD uncertainty of XANES analyses of Fe^{3+}/Fe_{tot}. Notably, within ~700 km of the Icelandic plume, the Fe^{3+}/Fe_{tot} ratio of natural samples clearly deviate from that of modelled partial melts. While Fe^{3+}/Fe_{tot} ratio in modelled partial melts decreases monotonically by 0.02-0.03 towards Iceland, the Reykjanes Ridge basalts remain nearly constant (Fig. 7a-b). The Fe^{3+}/Fe_{tot} ratio of the Reykjanes Ridge basalts at 400 km distance can be reproduced by melting DMM with a higher initial Fe^{3+}/Fe_{tot} content (6%, Fig. 8a). However, deviations from the models in both Fe^{3+}/Fe_{tot} and trace element ratios at approximately 700 km from Iceland require the mantle source heterogeneity, as is documented by radiogenic isotopes (e.g., Murton et al., 2002). For example, a difference of 0.02 Fe^{3+}/Fe_{tot} between natural and modelled melts is reached at 400 km distance (Fig. 8a), which is twice the conservative uncertainty of the XANES analyses (0.01 2SD). Shorttle et al. (2015) suggested that the presence of recycled, oxidized oceanic crust in the mantle sampled by the

543 Icelandic plume may explain the trace element and Fe^{3+}/Fe_{tot} signatures. The Fe^{3+}/Fe_{tot} ratios of the
544 Reykjanes Ridge basalts are therefore sensitive to the melting conditions and, importantly, to the
545 presence of chemical heterogeneities in the mantle source as observed in the northern part of the
546 ridge segment (Fig. 8a). The higher Fe^{3+}/Fe_{tot} signal observed in the Reykjanes Ridge basalts near
547 Iceland, compared to modelled concentrations of DMM with 5% Fe^{3+}/Fe_{tot}, can be explained by the
548 presence of pyroxenite in the source. Calculated partial melts of KG1 pyroxenite have high
549 Fe^{3+}/Fe_{tot} (up to 0.187, Table S5), which if mixed with melts produced from a nominal DMM
550 peridotite will counterbalance the Fe^{3+}/Fe_{tot} decrease predicted from T_p effects alone. Notably, the
551 more oxidized signature towards Iceland recognized by the Fe^{3+}/Fe_{tot} difference between the
552 Reykjanes Ridge basalts and the DMM model prediction is not recorded in the V/Sc ratios (Fig.
553 8b).
554
555 **4.4 The influence of a more oxidized and enriched source on the geochemistry of Reykjanes**
556 **Ridge basalts near Iceland**
557 The Nb/Zr concentrations of partial melts produced by DMM melting models (~0.03) are similar to
558 the Reykjanes Ridge basalts between 1100-700 km (Fig. 8c). However, Nb/Zr deviates from model
559 predictions at approximately 700 km and a ten-fold difference between the Reykjanes Ridge basalts
560 and the partial melts produced by DMM models is reached at 400 km (Fig. 8c). The deviation of
561 Nb/Zr ratios between the RR basalts and DMM models coincides with Fe^{3+}/Fe_{tot} mismatches (Fig.
562 S2), indicating the combined oxidized and enriched nature of the mantle source sampled by the
563 Reykjanes Ridge basalt close to Iceland.
564
565 In order to investigate the effect of lithological heterogeneity on Fe^{3+}/Fe_{tot} and trace elements used
566 as an indicator of enrichment, lavas from Stapafell were considered as a proxy for enriched melts.
567 Stapafell is one of the most enriched basalts on the Icelandic rift zone (Fig. 1) with high trace
568 element ratios (e.g., Nb/Zr= 0.157), high $^{87}Sr/^{86}Sr$ and low $^{143}Nd/^{144}Nd$ (e.g., Peate et al., 2009).

569 Importantly, Stapafell continues the geochemical trends towards Iceland set by the Reykjanes Ridge
570 basalts in the direction of progressively enriched compositions. Trace element concentrations of the
571 Reykjanes Ridge basalts range between partial melts produced by DMM melting models and
572 Stapafell lavas (Fig. 9), indicating that the apparent influence of an enriched source on approach to
573 Iceland is possibly the same that supplies Stapafell.
574
575 The composition of one of the Reykjanes Ridge basalts closest to Iceland at ~400 km (185D4,
576 Table S2), displays one of the highest deviations of Fe^{3+}/Fe_{tot} and Nb/Zr from the predictions of the
577 DMM melting models. The chemistry of 185D4 glass can be envisaged as a mixture of two melts,
578 one produced from ambient DMM and one from the enriched source of Stapafell lavas. This
579 simplification allows the composition of the enriched melt portion for sample 185D4 to be
580 calculated through mass balance, using the chemical composition of a Reykjanes Ridge basalt not
581 influenced by the plume (e.g., sample 12aD1 at ~1100 km; Table S2) as the melt produced by
582 melting DMM and normalizing the contributions from each melt to the crustal thickness. The
583 enriched melt composition calculated following this approach has a REE pattern that is similar to
584 Stapafell basalt (Fig. 10), also validating the choice of Stapafell to investigate enrichment along the
585 Reykjanes Ridge.
586
587 Pyroxenite melting models conducted here can reproduce some of the trace element contents of
588 Stapafell lavas (Table S5), suggesting that KG1 pyroxenite or similar lithologies may cause the
589 trace element enrichment towards Iceland, in agreement with Shorttle and Maclennan (2011). Low-
590 degree melts (F= 4-10 %) have Fe^{3+}/Fe_{tot}= 0.159-0.176, which if mixed with melts produced by
591 melting DMM, in a 1:1 ratio, replicate the Fe^{3+}/Fe_{tot} of the Reykjanes Ridge basalts at 400 km from
592 Iceland. The models developed in this study confirm the increasing contribution from a pyroxenitic
593 rich source towards Iceland along the Reykjanes Ridge, which increases incompatible trace element

concentrations and is required to counterbalance the modelled decreasing Fe^{3+}/Fe_{tot} of the basalts from a DMM source.

5. Conclusions

The behavior of V isotopes, V/Sc and Fe^{3+}/Fe_{tot} in the Reykjanes Ridge basalts can be summarized as follow:

1. Vanadium isotopic compositions do not systematically vary along the Reykjanes Ridge ($\delta^{51}V$= -0.97‰ ±0.17, n=19). $\delta^{51}V$ is not sensitive to the small fO_2 differences observed along the Reykjanes Ridge but may be controlled by the extent of melting when compared with global decompression melts (Wu et al., 2018). More studies on pristine basalts equilibrated at more extreme fO_2 conditions than those recorded along the Reykjanes Ridge are required to investigate the sensitivity of V isotopes to mantle fO_2. Vanadium isotopes appear insensitive to the presence of pyroxenite in the Reykjanes Ridge mantle source.

2. V/Sc ratios show a general increase towards Iceland due to fractional crystallization of clinopyroxene. High MgO basalts (> 7.5 wt%) not altered by crystallization show a minor decrease of V/Sc ratios along the Reykjanes Ridge towards Iceland that agree with melts produced by DMM melting models. However, V/Sc in the Reykjanes Ridge basalts does not increase towards Iceland where enriched and more oxidized mantle source is sampled by the basalts, suggesting that this proxy is not responsive to the presence of mantle chemical heterogeneities in these samples. The use of V/Sc as a fO_2 proxy is highly model-dependent, requiring independent constraints on source mineralogy, trace element abundance, extent of melting, and Tp. These parameters for Reykjanes Ridge lavas are sufficiently uncertain at this time to permit non-unique fO_2 determinations from measured V/Sc ratios.

620 3. Recalibrated Fe^{3+}/Fe_{tot} ratios, corrected for fractionation (MgO_{10}), remain virtually constant along
621 the Reykjanes Ridge. Thermodynamic melting models of DMM can reproduce Reykjanes Ridge
622 Fe^{3+} contents between 1100 and 700 km from the plume. However, melts produced upon melting
623 DMM need to be mixed with melts formed from an enriched source close to the plume, such as
624 pyroxenite, to replicate the Fe^{3+}/Fe_{tot} ratios observed between 400 and 700 km, which would
625 otherwise decrease under the influence of increased mantle potential temperature. Basalt
626 Fe^{3+}/Fe_{tot} both depends on melting conditions (T_p) and is responsive to bulk oxidation state
627 alterations associated with the presence of chemical heterogeneities in the mantle.
628
629 **Acknowledgments**
630 This study was funded by the Natural Environment Research Council NERC grant NE/N009568/1
631 to J.M. and J.P. Katharina Kreissig and Barry Coles are thanked for their help in conducting the V
632 isotopes work. Thanks also to Jason Day for the support in performing the LA-ICPMS analyses. OS
633 acknowledges Diamond Light Source for time on beamline I18 under proposals SP9446, SP9456
634 and SP12130 and the support during our analytical sessions from beamline scientist Konstantin
635 Ignatyev and principal beamline scientist Fred Mosselmans. This manuscript greatly benefitted
636 from comments of an anonymous reviewer and a very careful revision of Maryjo Brounce
637 especially with regards to the XANES and Fe^{3+}/Fe_{tot} calibration debate.
638
639 **References**
640 Asimow, P.D., Ghiorso, M.S., 1998. Algorithmic modifications extending MELTS to calculate
641 subsolidus phase relations. Am. Mineral. 83, 1127–1132. https://doi.org/10.2138/am-1998-9-
642 1022
643 Bach, W., Bernhard, P.E., Hart, S.R., Blusztajn, J.S., 2003. Geochemistry of hydrothermally altered
644 oceanic crust: DSDP/ODP Hole 504B-Implications for seawater-crust exchange budgets and
645 Sr-and Pb-isotopic evolution of the mantle. Geochemistry, Geophys. Geosystems 4, 40–55.

https://doi.org/10.1029/2002GC000419

Berry, A.J., Stewart, G.A., O'Neill, H.S.C., Mallmann, G., Mosselmans, J.F.W., 2018. A re-assessment of the oxidation state of iron in MORB glasses. Earth Planet. Sci. Lett. 483, 114–123. https://doi.org/10.1016/j.epsl.2017.11.032

Birner, S.K., Cottrell, E., Warren, J.M., Kelley, K.A., Davis, F.A., 2018. Peridotites and basalts reveal broad congruence between two independent records of mantle fO2 despite local redox heterogeneity. Earth Planet. Sci. Lett. 494, 172–189. https://doi.org/10.1016/j.epsl.2018.04.035

Brounce, M., Kelley, K.A., Cottrell, E., Reagan, M.K., 2015. Temporal evolution of mantle wedge oxygen fugacity during subduction initiation. Geology 43, 775–778. https://doi.org/10.1130/G36742.1

Brounce, M., Stolper, E., Eiler, J., 2017. Redox variations in Mauna Kea lavas, the oxygen fugacity of the Hawaiian plume, and the role of volcanic gases in Earth's oxygenation. Proc. Natl. Acad. Sci. 114, 8997–9002. https://doi.org/10.1073/pnas.1619527114

Brounce, M.N., Kelley, K.A., Cottrell, E., 2014. Variations in Fe3+/PFe of Mariana Arc Basalts and MantleWedge fO2. J. Petrol. 55, 2514–2536. https://doi.org/10.1093/petrology/egu065

Bucholz, C.E., Kelemen, P.B., 2019. Oxygen fugacity at the base of the Talkeetna arc, Alaska. Contrib. to Mineral. Petrol. 174, 1–27. https://doi.org/10.1007/s00410-019-1609-z

Canil, D., 1999. Vanadium partitioning between orthopyroxene, spinel and silicate melt and the redox states of mantle source regions for primary magmas. Geochim. Cosmochim. Acta 63, 557–572. https://doi.org/10.1016/S0016-7037(98)00287-7

Canil, D., 1997. Vanadium partitioning and the oxidation state of Archaean komatiite magmas. Nature 389, 842–845.

Canil D., O'Neill H. C., 1996. Distribution of Ferric Iron in some Upper-Mantle Assemblages . J. Petrol. 37, 609–635.

Cottrell, E., Kelley, K.A., 2013. Redox heterogeneity in mid-ocean ridge basalts as a function of mantle source. Science 340, 1314–1317. https://doi.org/10.1126/science.1233299

672 Cottrell, E., Kelley, K.A., 2011. The oxidation state of Fe in MORB glasses and the oxygen
673 fugacity of the upper mantle. Earth Planet. Sci. Lett. 305, 270–282.
674 https://doi.org/10.1016/j.epsl.2011.03.014
675 Cottrell, E., Kelley, K.A., Lanzirotti, A., Fischer, R.A., 2009. High-precision determination of iron
676 oxidation state in silicate glasses using XANES. Chem. Geol. 268, 167–179.
677 https://doi.org/10.1016/j.chemgeo.2009.08.008
678 Davis, F.A., Cottrell, E., 2018. Experimental investigation of basalt and peridotite oxybarometers:
679 Implications for spinel thermodynamic models and Fe3+ compatibility during generation of
680 upper mantle melts. Am. Mineral. 103, 1056–1067. https://doi.org/10.2138/am-2018-6280
681 Frost, D.J., McCammon, C.A., 2008. The Redox State of Earth's Mantle. Annu. Rev. Earth Planet.
682 Sci. 36, 389–420. https://doi.org/10.1146/annurev.earth.36.031207.124322
683 Frost, R.B., 1991. Introduction to oxygen fugacity and its petrologic importance, in: Reviews in
684 Mineralogy & Geochemistry 25. pp. 1–10.
685 Gaetani, G.A., 2016. The behavior of Fe 3+ /∑Fe during partial melting of spinel lherzolite.
686 Geochim. Cosmochim. Acta 185, 64–77. https://doi.org/10.1016/j.gca.2016.03.019
687 Gaillard, F., Scaillet, B., Arndt, N.T., 2011. Atmospheric oxygenation caused by a change in
688 volcanic degassing pressure. Nature 478, 229–232. https://doi.org/10.1038/nature10460
689 Gale, A., Dalton, C.A., Langmuir, C.H., Su, Y., Schilling, J.G., 2013. The mean composition of
690 ocean ridge basalts, Geochemistry, Geophysics, Geosystems.
691 https://doi.org/10.1029/2012GC004334
692 Ghiorso, M.S., Hirschmann, M.M., Reiners, P.W., Kress, V.C., 2002. The pMELTS: A revision of
693 MELTS for improved calculation of phase relations and major element partitioning related to
694 partial melting of the mantle to 3 GPa. Geochemistry, Geophys. Geosystems 3, 1–35.
695 https://doi.org/10.1029/2001GC000217
696 Hartley, M.E., Shorttle, O., Maclennan, J., Moussallam, Y., Edmonds, M., 2017. Olivine-hosted
697 melt inclusions as an archive of redox heterogeneity in magmatic systems. Earth Planet. Sci.

Lett. 479, 192–205. https://doi.org/10.1016/j.epsl.2017.09.029

Helz, R.T., Cottrell, E., Brounce, M.N., Kelley, K.A., 2017. Olivine-melt relationships and syneruptive redox variations in the 1959 eruption of Kīlauea Volcano as revealed by XANES. J. Volcanol. Geotherm. Res. 333–334, 1–14. https://doi.org/10.1016/j.jvolgeores.2016.12.006

Hopkins, S.S., Prytulak, J., Barling, J., Russell, S.S., Coles, B.J., Halliday, A.N., 2019. The vanadium isotopic composition of lunar basalts. Earth Planet. Sci. Lett. 511, 12–24. https://doi.org/10.1016/j.epsl.2019.01.008

Jones, S.M., Murton, B.J., Fitton, J.G., White, N.J., Maclennan, J., Walters, R.L., 2014. A joint geochemical-geophysical record of time-dependent mantle convection south of Iceland. Earth Planet. Sci. Lett. 386, 86–97. https://doi.org/10.1016/j.epsl.2013.09.029

Kelley, K.A., Cottrell, E., 2012. The influence of magmatic differentiation on the oxidation state of Fe in a basaltic arc magma. Earth Planet. Sci. Lett. 329–330, 109–121. https://doi.org/10.1016/j.epsl.2012.02.010

Kelley, K.A., Cottrell, E., 2009. Water and the oxidation state of subduction zone magmas. Science 325, 605–607.

Klein, E.M., Langmuir, C.H., 1987. Global Correlations of Ocean Ridge Basalt Chemistry with Axial Depth and Crustal Thickness. J. Geophys. Res. 92, 8089–8115.

Kogiso, T., Hirose, K., Takahashi, E., 1998. Melting experiments on homogeneous mixtures of peridotite and basalt: Application to the genesis of ocean island basalts. Earth Planet. Sci. Lett. 162, 45–61. https://doi.org/10.1016/S0012-821X(98)00156-3

Kress, V.C., Carmichael, I.S.E., 1991. The compressibility of silicate liquids containing Fe2O3 and the effect of composition, temperature, oxygen fugacity and pressure on their redox state. Contrib. to Mineral. Petrol. 108, 82–92.

Laubier, M., Grove, T.L., Langmuir, C.H., 2014. Trace element mineral/melt partitioning for basaltic and basaltic andesitic melts: An experimental and laser ICP-MS study with application to the oxidation state of mantle source regions. Earth Planet. Sci. Lett. 392, 265–278.

724 https://doi.org/10.1016/j.epsl.2014.01.053
725 Lee, C.T.A., Brandon, A.D., Norman, M., 2003. Vanadium in peridotites as a proxy for paleo-fO2
726 during partial melting: Prospects, limitations, and implications. Geochim. Cosmochim. Acta
727 67, 3045–3064. https://doi.org/10.1016/S0016-7037(00)00268-0
728 Lee, C.T.A., Leeman, W.P., Canil, D., Li, Z.X.A., 2005. Similar V/Sc systematics in MORB and
729 arc basalts: Implications for the oxygen fugacities of their mantle source regions. J. Petrol. 46,
730 2313–2336. https://doi.org/10.1093/petrology/egi056
731 Li, Z.X.A., Lee, C.T.A., 2004. The constancy of upper mantle fO 2 through time inferred from V/Sc
732 ratios in basalts. Earth Planet. Sci. Lett. 228, 483–493.
733 https://doi.org/10.1016/j.epsl.2004.10.006
734 Mallmann, G., O'Neill, H.S.C., 2013. Calibration of an empiricalthermometer and oxybarometer
735 based on the partitioning of sc, Y and V between olivine and silicate melt. J. Petrol. 54, 933–
736 949. https://doi.org/10.1093/petrology/egt001
737 Mallmann, G., O'Neill, H.S.C., 2009. The crystal/melt partitioning of V during mantle melting as a
738 function of oxygen fugacity compared with some other elements (Al, P, Ca, Sc, Ti, Cr, Fe, Ga,
739 Y, Zr and Nb). J. Petrol. 50, 1765–1794. https://doi.org/10.1093/petrology/egp053
740 Matthews, S., Shorttle, O., Maclennan, J., 2016. The temperature of the Icelandic mantle from
741 olivine-spinel aluminum exchange thermometry. Geochemistry Geophys. Geosystems 17,
742 4725–4752. https://doi.org/10.1002/ 2016GC006497
743 M^{c}kenzie, D., O'nions, R.K., 1995. The source regions of ocean island basalts. J. Petrol. 36, 133–
744 159. https://doi.org/10.1093/petrology/36.1.133
745 M^{c}Kenzie, D., O'Nions, R.K., 1991. Partial melt coefficients from inversion of rare earth element
746 concentrations. J. Petrol. 23, 1021–1091.
747 https://doi.org/http://dx.doi.org/10.1093/petrology/32.5.1021
748 Moussallam, Y., Edmonds, M., Scaillet, B., Peters, N., Gennaro, E., Sides, I., Oppenheimer, C.,
749 2016. The impact of degassing on the oxidation state of basaltic magmas: A case study of

Kīlauea volcano. Earth Planet. Sci. Lett. 450, 317–325. https://doi.org/10.1016/j.epsl.2016.06.031

Moussallam, Y., Oppenheimer, C., Scaillet, B., Gaillard, F., Kyle, P., Peters, N., Hartley, M., Berlo, K., Donovan, A., 2014. Tracking the changing oxidation state of Erebus magmas, from mantle to surface, driven by magma ascent and degassing. Earth Planet. Sci. Lett. 393, 200–209. https://doi.org/10.1016/j.epsl.2014.02.055

Murton, B.J., Taylor, R.N., Thirlwall, M.F., 2002. Plume-Ridge Interaction: a Geochemical Perspective from the Reykjanes Ridge. J. Petrol. 43, 1987–2012. https://doi.org/10.1093/petrology/43.11.1987

Nielsen, S.G., Prytulak, J., Halliday, A.N., 2011. Determination of Precise and Accurate 51V/50V Isotope Ratios by MC-ICP-MS, Part 1: Chemical Separation of Vanadium and Mass Spectrometric Protocols. Geostand. Geoanalytical Res. 35, 293–306. https://doi.org/10.1111/j.1751-908x.2011.00106.x

O'Neill, H.S.C., Berry, A.J., Mallmann, G., 2018. The oxidation state of iron in Mid-Ocean Ridge Basaltic (MORB) glasses: Implications for their petrogenesis and oxygen fugacities. Earth Planet. Sci. Lett. 504, 152–162. https://doi.org/10.1016/j.epsl.2018.10.002

O'Neill, H.S.C., Wall, V.J., 1987. The olivine-orthopyroxene-spinel oxygen geobarometer, the nickel precipitation curve, and the oxygen fugacity of the earth's upper mantle. J. Petrol. 28, 1169–1191.

Peate, D.W., Baker, J.A., Jakobsson, S.P., Waight, T.E., Kent, A.J.R., Grassineau, N. V., Skovgaard, A.C., 2009. Historic magmatism on the Reykjanes Peninsula, Iceland: A snap-shot of melt generation at a ridge segment. Contrib. to Mineral. Petrol. 157, 359–382. https://doi.org/10.1007/s00410-008-0339-4

Prytulak, J., Nielsen, S.G., Ionov, D.A., Halliday, A.N., Harvey, J., Kelley, K.A., Niu, Y.L., Peate, D.W., Shimizu, K., Sims, K.W.W., 2013. The stable vanadium isotope composition of the mantle and mafic lavas. Earth Planet. Sci. Lett. 365, 177–189.

776 https://doi.org/10.1016/j.epsl.2013.01.010
777 Prytulak, J., Sossi, P.A., Halliday, A.N., Plank, T., Savage, P.S., Woodhead, J.D., 2017. Stable
778 vanadium isotopes as a redox proxy in magmatic systems? Geochemical Perspect. Lett. 75–84.
779 https://doi.org/10.7185/geochemlet.1708
780 Rouxel, O., Dobbek, N., Ludden, J., Fouquet, Y., 2003. Iron isotope fractionation during oceanic
781 crust alteration. Chem. Geol. 202, 155–182. https://doi.org/10.1016/j.chemgeo.2003.08.011
782 Rudge, J.F., Maclennan, J., Stracke, A., 2013. The geochemical consequences of mixing melts from
783 a heterogeneous mantle. Geochim. Cosmochim. Acta 114, 112–143.
784 https://doi.org/10.1016/j.gca.2013.03.042
785 Salters, V.J.M., Stracke, A., 2004. Composition of the depleted mantle. Geochemistry, Geophys.
786 Geosystems 5. https://doi.org/10.1029/2003GC000597
787 Schilling, JG, 1973. Iceland Mantle Plume: Geochemical study of Reykjanes Ridge. Nature 242,
788 565–571.
789 Shorttle, O., Maclennan, J., 2011. Compositional trends of Icelandic basalts: Implications for short-
790 length scale lithological heterogeneity in mantle plumes. Geochemistry, Geophys. Geosystems
791 12. https://doi.org/10.1029/2011GC003748
792 Shorttle, O., MacLennan, J., Jones, S.M., 2010. Control of the symmetry of plume-ridge interaction
793 by spreading ridge geometry. Geochemistry, Geophys. Geosystems 11, 1–27.
794 https://doi.org/10.1029/2009GC002986
795 Shorttle, O., Moussallam, Y., Hartley, M.E., Maclennan, J., Edmonds, M., Murton, B.J., 2015. Fe-
796 XANES analyses of Reykjanes Ridge basalts: Implications for oceanic crust's role in the solid
797 Earth oxygen cycle. Earth Planet. Sci. Lett. 427, 272–285.
798 https://doi.org/10.1016/j.epsl.2015.07.017
799 Sims, K.W.W., Depaolo, D.J., Murrell, M.T., Baldridge, W.S., Goldstein, S., Clague, D., Jull, M.,
800 1999. Porosity of the melting zone and variations in the solid mantle upwelling rate beneath
801 Hawaii: Inferences from 238U-230Th-226Ra and 235U-231Pa disequilibria. Geochim.

802 Cosmochim. Acta 63, 4119–4138.
803 Smith, P.M., Asimow, P.D., 2005. Adiabat-1ph: A new public front-end to the MELTS, pMELTS,
804 and pHMELTS models. Geochemistry, Geophys. Geosystems 6, 1–8.
805 https://doi.org/10.1029/2004GC000816
806 Sossi, P.A., Prytulak, J., O'Neill, H.S.C., 2018. Experimental calibration of vanadium partitioning
807 and stable isotope fractionation between hydrous granitic melt and magnetite at 800 °C and
808 0.5 GPa. Contrib. to Mineral. Petrol. 173, 0. https://doi.org/10.1007/s00410-018-1451-8
809 Stolper, D.A., Keller, C.B., 2018. A record of deep-ocean dissolved O2 from the oxidation state of
810 iron in submarine basalts. Nature 553, 323–327. https://doi.org/10.1038/nature25009
811 Stracke, A., Bizimis, M., Salters, V.J.M., 2003. Recycling oceanic crust: Quantitative constraints.
812 Geochemistry, Geophys. Geosystems 4. https://doi.org/10.1029/2001GC000223
813 Teng, F.-Z., Dauphas, N., Watkins, J.M., 2017. Non-Traditional Stable Isotopes: Retrospective and
814 Prospective, in: Reviews in Mineralogy & Geochemistry. pp. 1–26.
815 https://doi.org/10.2138/rmg.2017.82.1
816 Workman, R.K., Hart, S.R., 2005. Major and trace element composition of the depleted MORB
817 mantle (DMM). Earth Planet. Sci. Lett. 231, 53–72. https://doi.org/10.1016/j.epsl.2004.12.005
818 Wu, F., Qi, Y., Perfit, M.R., Gao, Y., Langmuir, C.H., Wanless, V.D., Yu, H., Huang, F., 2018.
819 Vanadium isotope compositions of mid-ocean ridge lavas and altered oceanic crust. Earth
820 Planet. Sci. Lett. 493, 128–139. https://doi.org/10.1016/j.epsl.2018.04.009
821 Zhang, H.L., Cottrell, E., Solheid, P.A., Kelley, K.A., Hirschmann, M.M., 2018. Determination of
822 Fe3 +/ΣFe of XANES basaltic glass standards by Mössbauer spectroscopy and its application
823 to the oxidation state of iron in MORB. Chem. Geol. 479, 166–175.
824 https://doi.org/10.1016/j.chemgeo.2018.01.006
825 Zhang, H.L., Hirschmann, M.M., Cottrell, E., Newville, M., Lanzirotti, A., 2016. Structural
826 environment of iron and accurate determination of Fe3+/σFe ratios in andesitic glasses by
827 XANES and Mössbauer spectroscopy. Chem. Geol. 428, 48–58.

https://doi.org/10.1016/j.chemgeo.2016.02.022

Figure captions

Fig. 1: Map showing the location of the Reykjanes Ridge basalts investigated in this study (dark blue circles indicating samples with Fe^{3+}/Fe_{tot} and V/Sc data, light blue circles showing those with additional V isotopic compositions). Stapafell eruption on the Reykjanes Peninsula (coral circle) and the plume center location (white star) proposed by Shorttle et al. (2010) are also shown. The map was prepared with the software GeoMapApp (www.geomapapp.org).

Fig. 2: Vanadium isotopes along the investigated spread of the Reykjanes Ridge, reported as $\delta^{51}V$, plotted as a function of MgO content (Shorttle et al., 2015). The grey horizontal bar indicates the average MORB value of Wu et al. (2018) with calculated 2SD.

Fig.3: Vanadium isotopic composition plotted against (**a**) Fe^{3+}/Fe_{tot} (corrected to MgO_{10}, see text) and (**b**) V/Sc. Circles are color coded as a function of MgO content measured by electron microprobe (Shorttle et al., 2015).

Fig. 4: Na_8 vs $\delta^{51}V$ of the Reykjanes Ridge lavas investigated in this study (circles). Ridge segments data from Wu et al. (2018) and Prytulak et al. (2013) are also plotted as diamonds (Na_8 data reported in Wu et al., 2018). Na_8 values for the Reykjanes Ridge samples were calculated from the regressed melt compositions at ~8 wt% MgO (see text) using the formula of Shorttle et al. (2010). The grey horizontal bar indicates the average MORB value of Wu et al. (2018) with calculated 2SD.

Fig. 5: The V/Sc ratio of the Reykjanes Ridge basalts as a function of distance from the Icelandic plume. Samples are color coded with the MgO content (Shorttle et al., 2015), highlighting the effect

of fractional crystallization. Errors of the V/Sc ratios were calculated from the errors on V and Sc (LA-ICPMS analyses; Supplementary Table S2) and range between 0.11 and 1.29 1SD.

Fig. 6: CaO vs MgO content of the Reykjanes Ridge basalts as a function of V/Sc ratio.

Fig. 7: Fe^{3+}/Fe_{tot} ratio and oxygen fugacity along the Reykjanes Ridge. (**a**) Raw Fe^{3+}/Fe_{tot} ratios recalculated from the study of Shorttle et al. (2015) using the new calibration of the XANES standards (Zhang et al., 2018; see text). Data are plotted as a function of MgO content of the glasses (Shorttle et al., 2015). (**b**) Fe^{3+}/Fe_{tot} ratios of the same samples in (**a**) but now corrected for fractional crystallization to MgO_{10} (see text), as a function of Nb/Zr. (**c**) Oxygen fugacity, as $\log_{}fO_2$ relative to the FMQ buffer (Frost, 1991), calculated from the data in (**b**) using the calibration of Kress and Carmichael (1991) at 2 kb and 1200 °C. Data are plotted as a function of Nb/Zr of the glasses.

Fig. 8: Reykjanes Ridge basalt (blue circles) plotted as a function of distance from the Icelandic plume along with partial melt compositions produced by the thermodynamic melting models of DMM with 4, 5 and 6% Fe^{3+}/Fe_{tot} in the source (grey circles). (**a**) Fe^{3+}/Fe_{tot} ratios of basalt corrected to MgO_{10}. (**b**) V/Sc ratios, where light blue circles indicate more evolved basalts (< 7.5 wt% MgO) and dark blue circles indicate more primitive compositions (> 7.5 wt% MgO). (**c**) Nb/Zr ratios, with concentrations of the different models overlapping and being indistinguishable at the scale of the plot. Pale red arrows in panel (**a**) and (**c**) highlight the disparity between Reykjanes Ridge basalts and DMM modelled compositions near Iceland.

Fig. 9: Ba and La compositional trend of Reykjanes Ridge basalts (blue) between partial melts produced by DMM melting model with 5% initial Fe^{3+}/Fe_{tot} (grey) and Stapafell basalt from the Reykjanes Peninsula (coral).

880

881 **Fig. 10**: Spider diagram reporting the trace element composition of Stapafell basaltic glass (Peate et
882 al., 2009), in coral, and the enriched melt forming at the point closest to the Icelandic plume along
883 the Reykjanes Ridge, in blue. In grey and yellow are also represented the compositions of
884 Reykjanes Ridge basalts 12aD1 (~1100 from Iceland) and 185D4 (~ 400 km from Iceland),
885 respectively, used to mass balance the enriched melt composition. See text for more details.

886

887 **Fig. S1**: Fractional crystallization model for Reykjanes Ridge basalt 153D3. The melt concentration
888 was calculated at an arbitrary low pressure of 0.6 kb using MELTS (Ghiorso et al., 2002; Smith and
889 Asimow, 2005). The model shows that V/Sc ratios in melts with MgO >7.5 wt% are not affected by
890 crystallization. Calculations employed D_V and D_{Sc} at FMQ from Mallmann and O'Neill (2009,
891 2013). Between 9 and 7.5 wt% MgO only olivine crystallizes, while clinopyroxene (cpx) and
892 plagioclase (plag) start to crystallize at ~7.5 and ~6 wt% MgO, respectively.

893

894 **Fig. S2**: Difference in Fe^{3+}/Fe_{tot} between the Reykjanes Ridge basalt and the partial melt
895 composition produced by DMM melting model with 5% initial Fe^{3+}/Fe_{tot} ($\Delta Fe^{3+}/Fe_{tot}$), calculated at
896 a particular distance, against the Nb/Zr ratio of the Reykjanes Ridge basalts.

Figure1
Click here to download Figure: RR-Fig.1.pdf

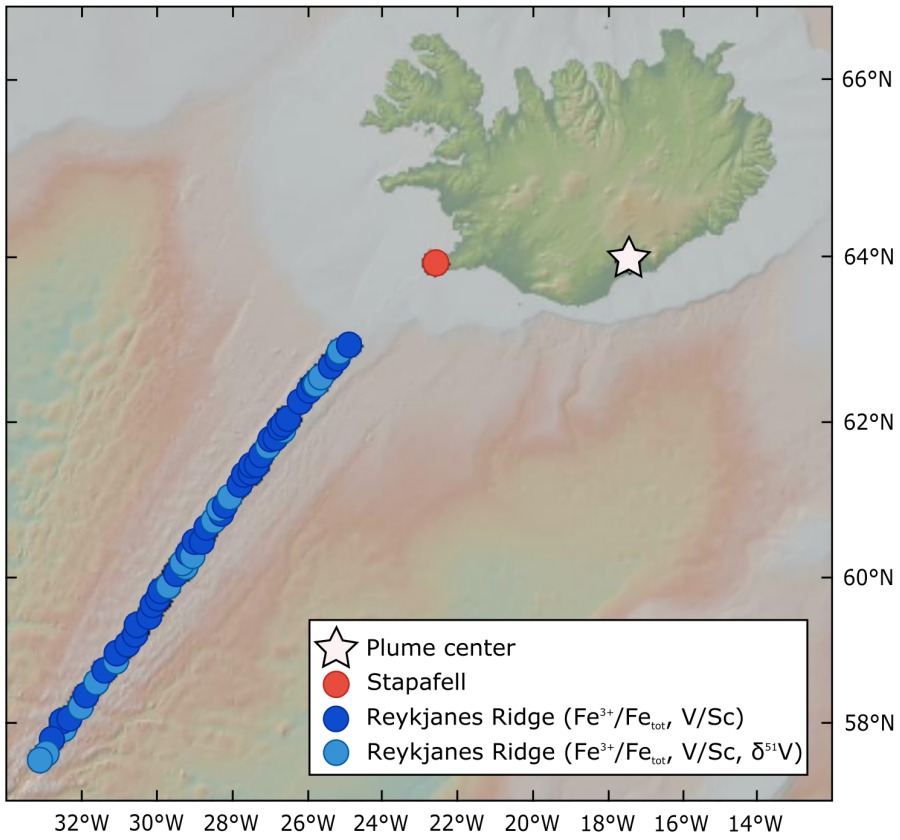

Figure2
Click here to download Figure: Fig.2-new.pdf

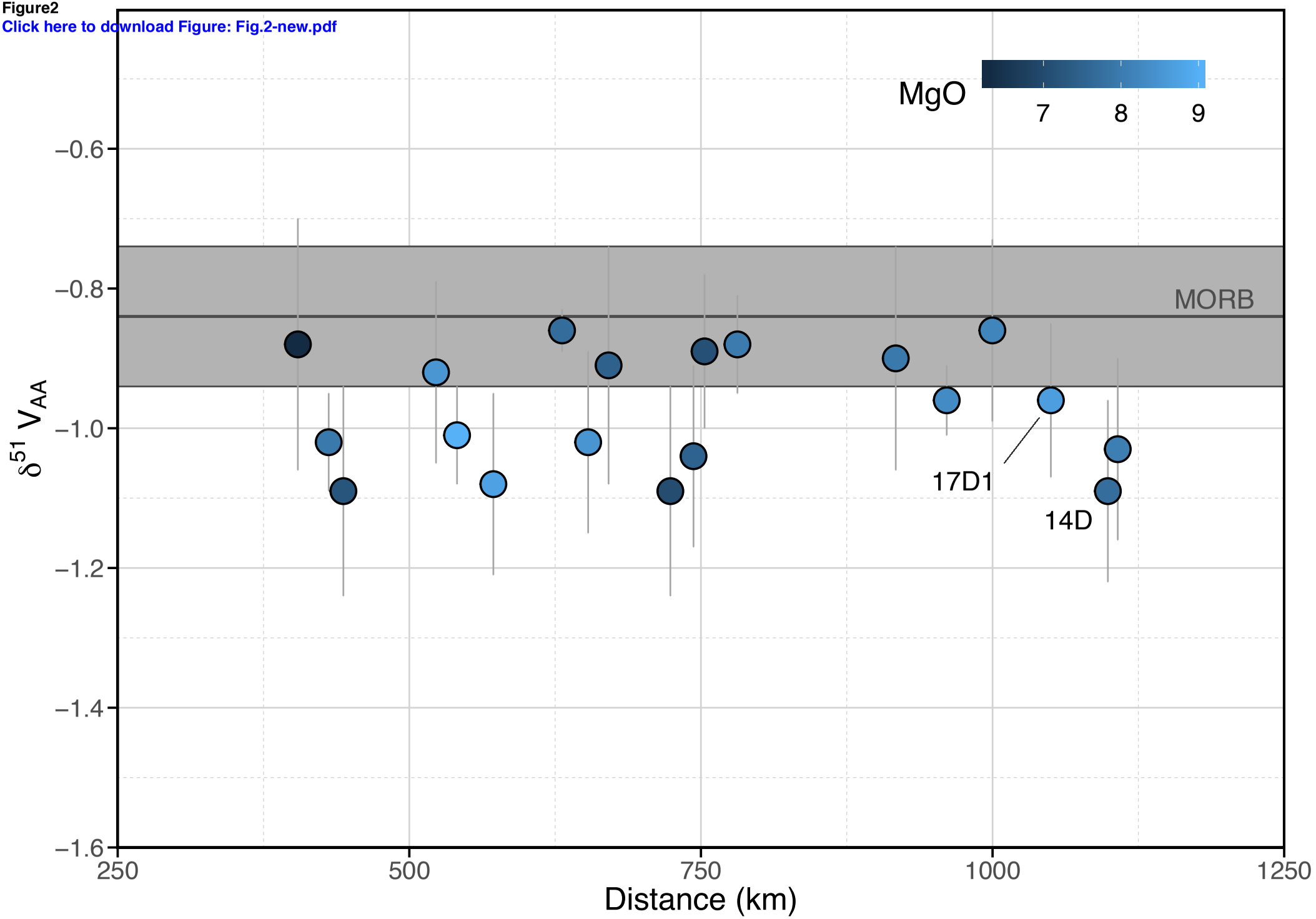

Figure3
Click here to download Figure: Fig.3-new.pdf

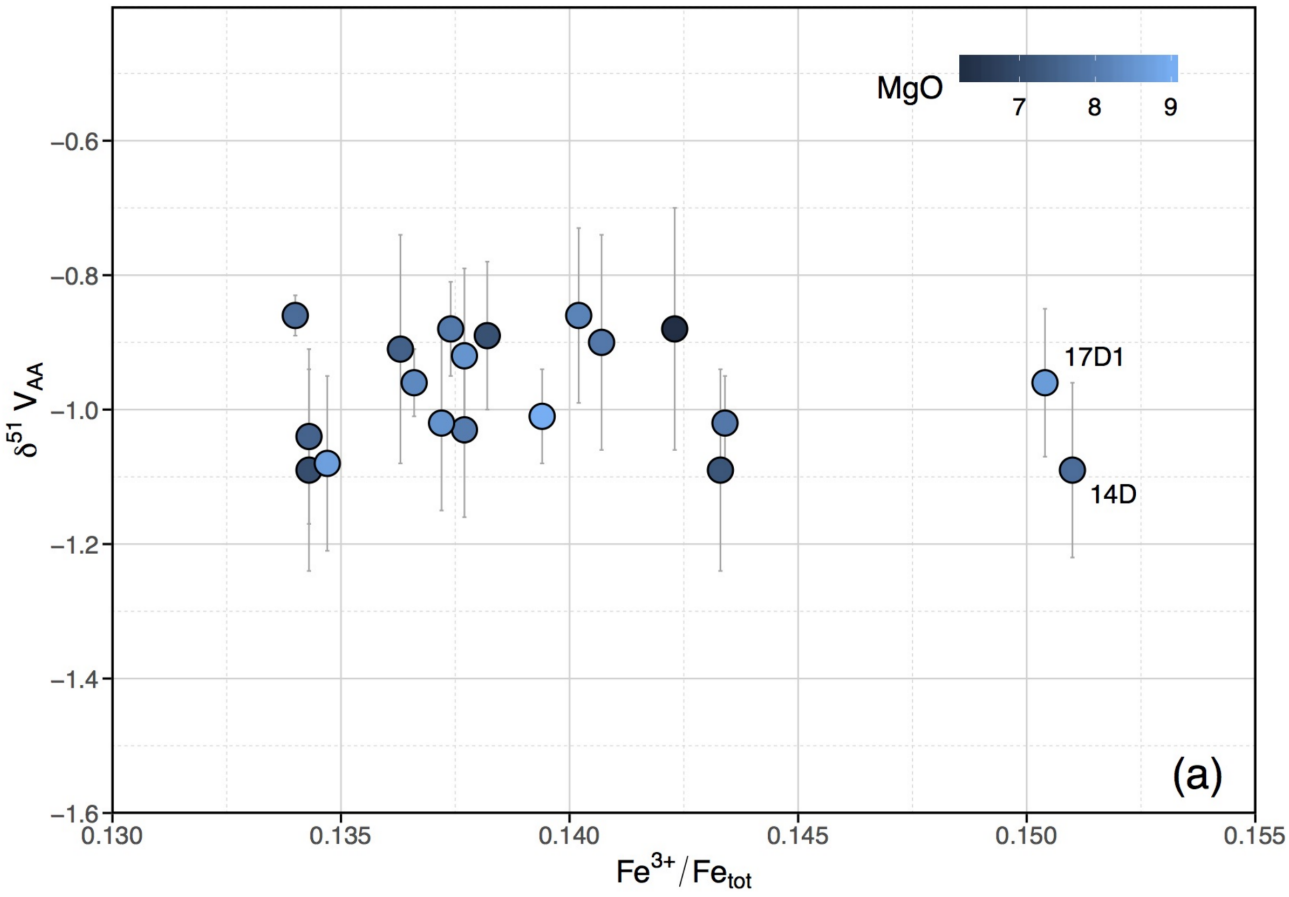

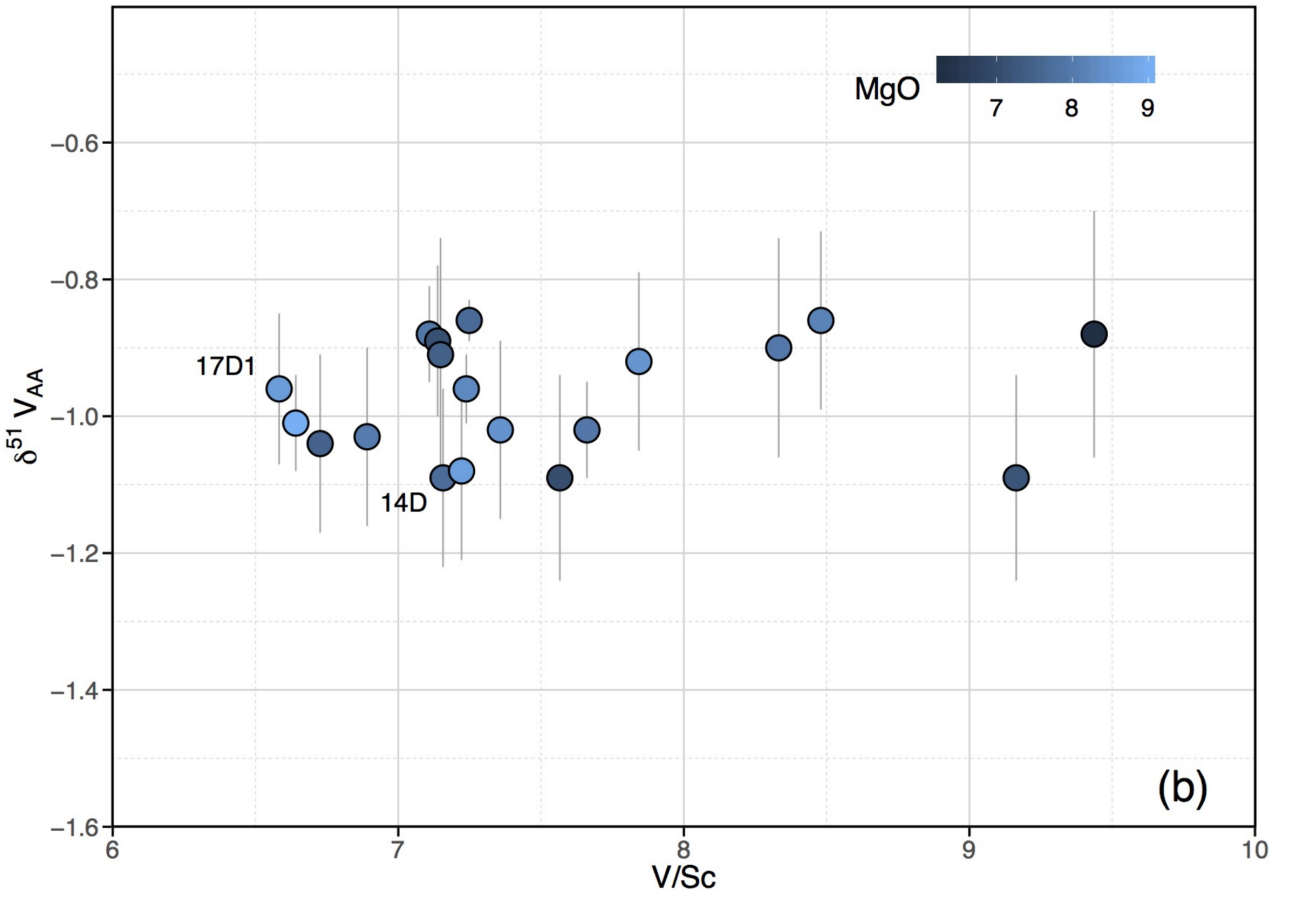

Figure4
Click here to download Figure: Fig.4-new.pdf

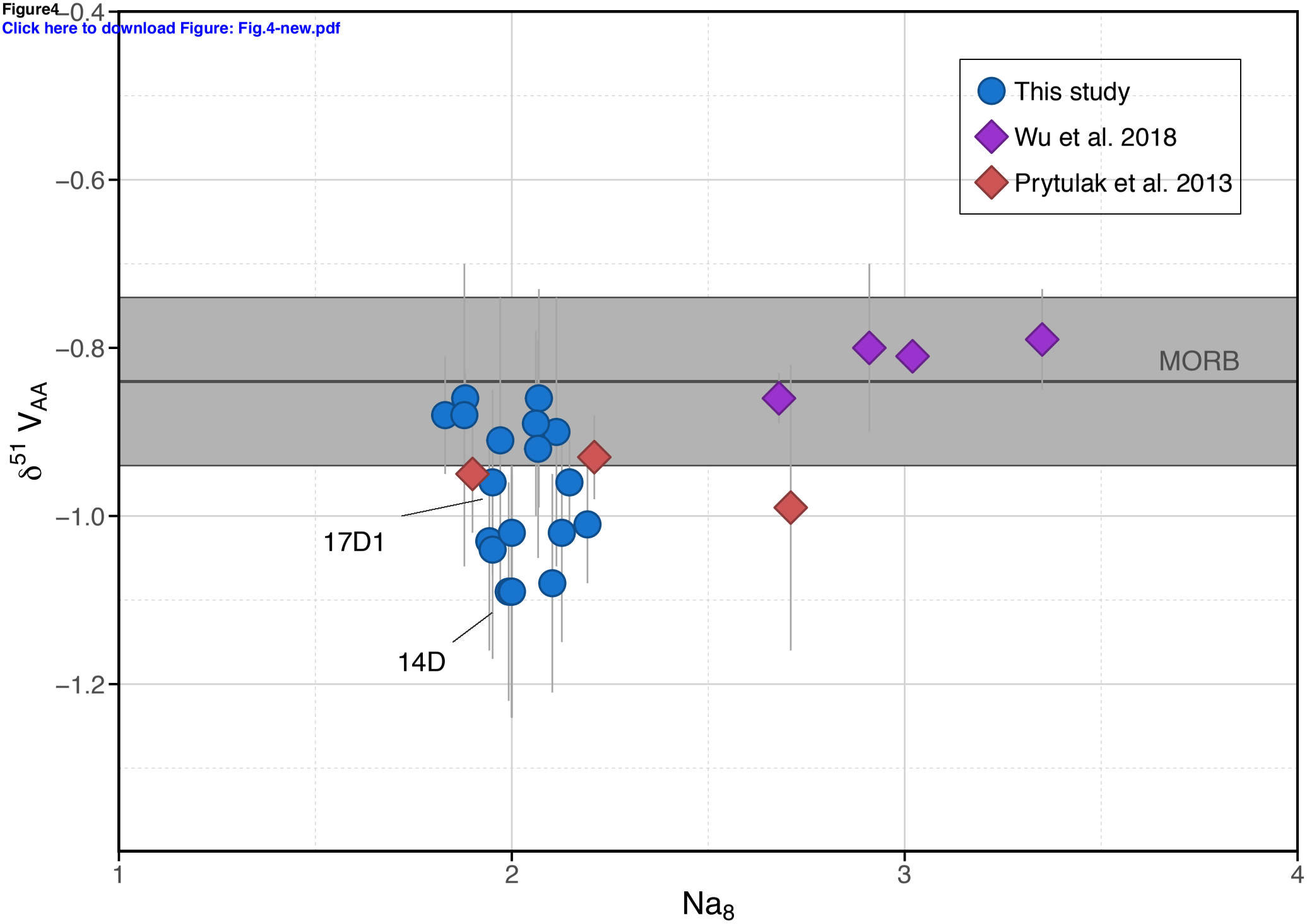

Figure5
Click here to download Figure: Fig.5-new.pdf

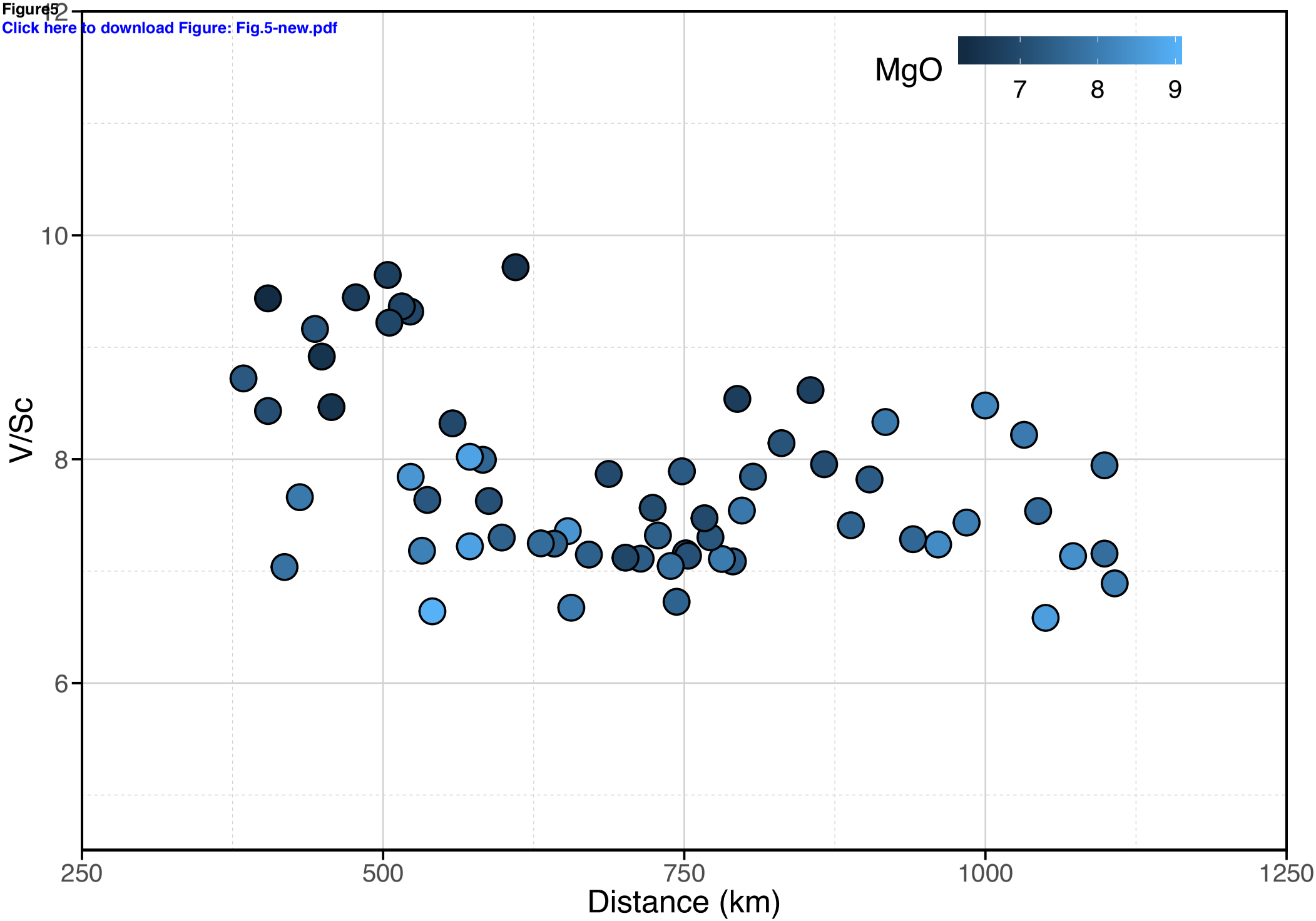

Figure6
Click here to download Figure: Fig.6-new.pdf

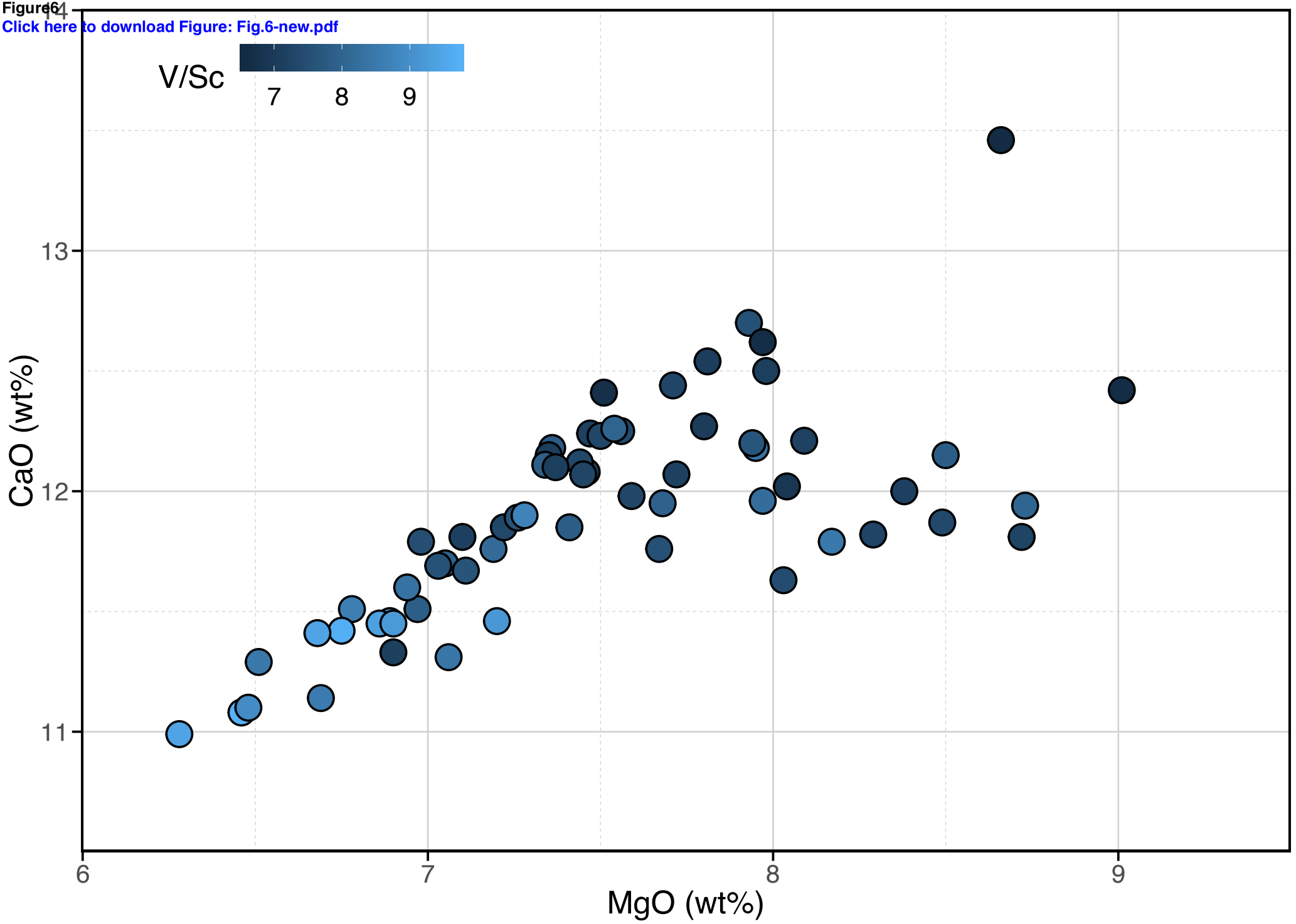

Figure7

Click here to download Figure: Fig.7-new.pdf

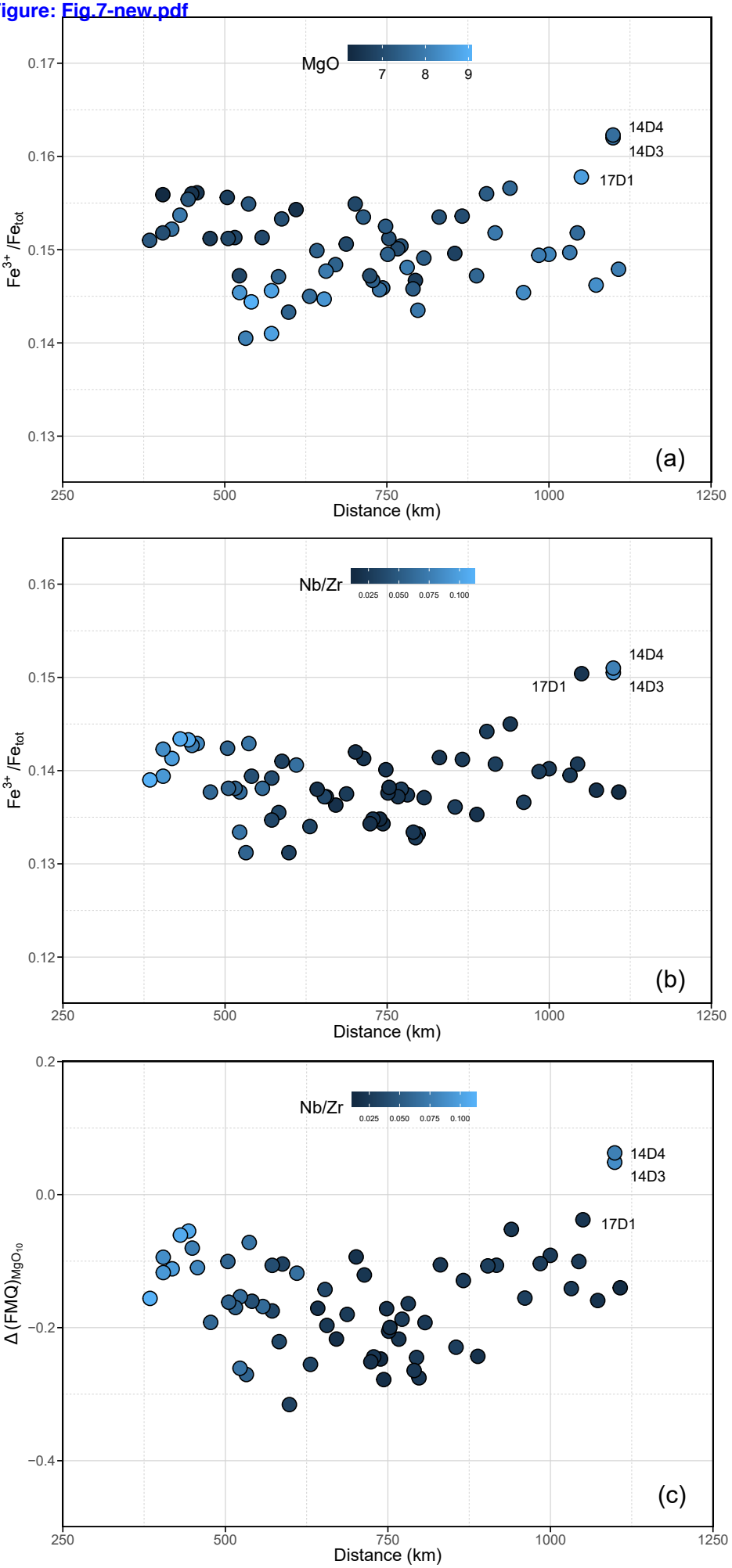

Figure8

Click here to download Figure: Fig.8-new.pdf

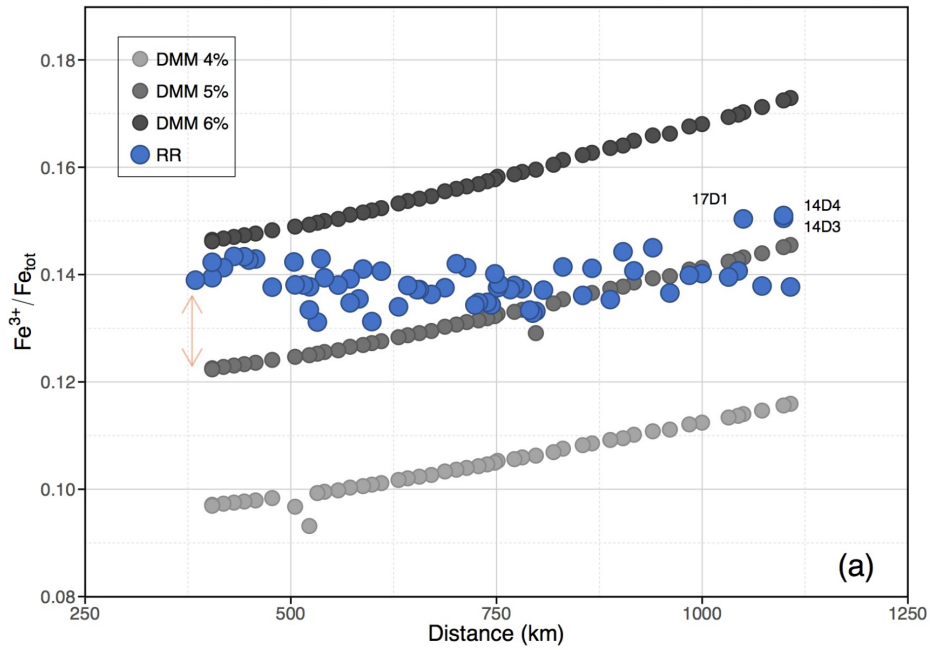

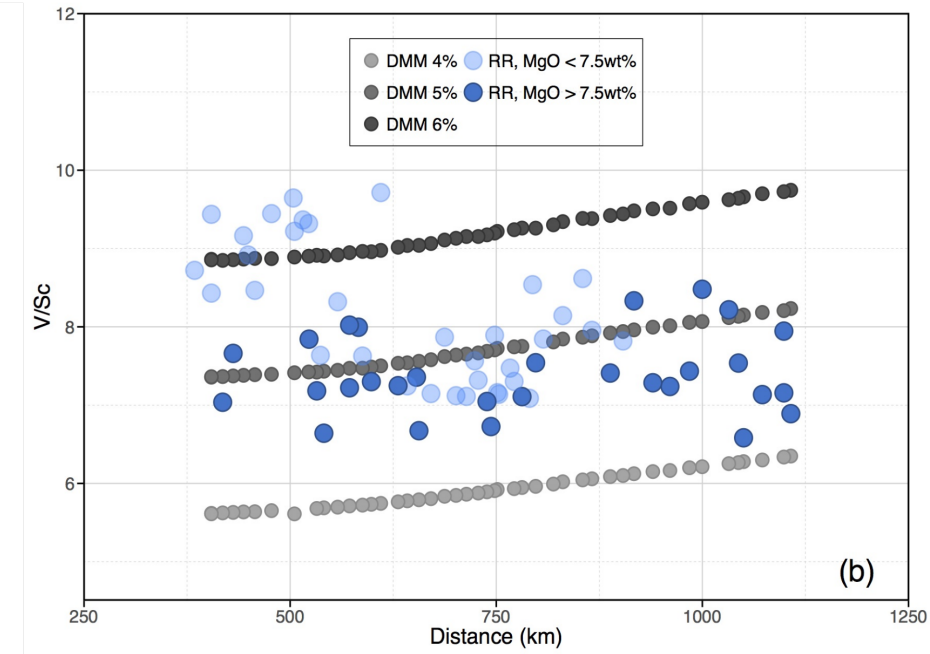

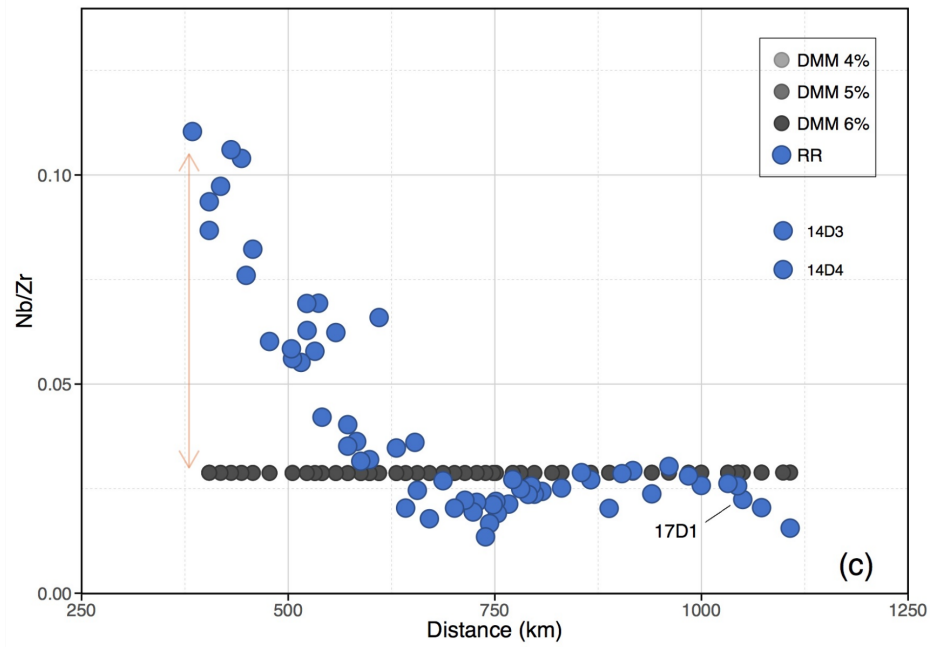

Figure9
Click here to download Figure: Fig.9-new.pdf

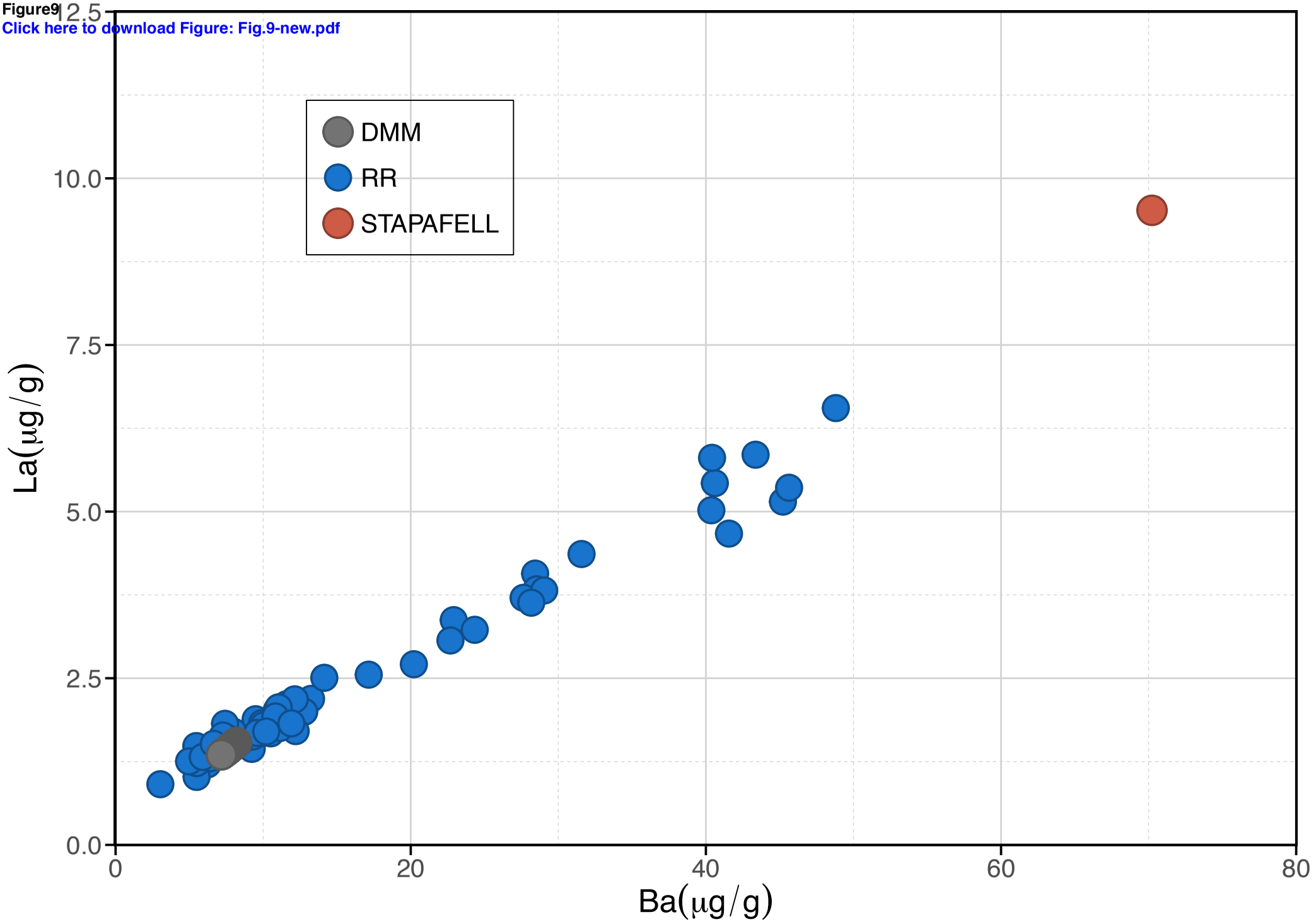

Figure10
Click here to download Figure: Fig.10-new.pdf

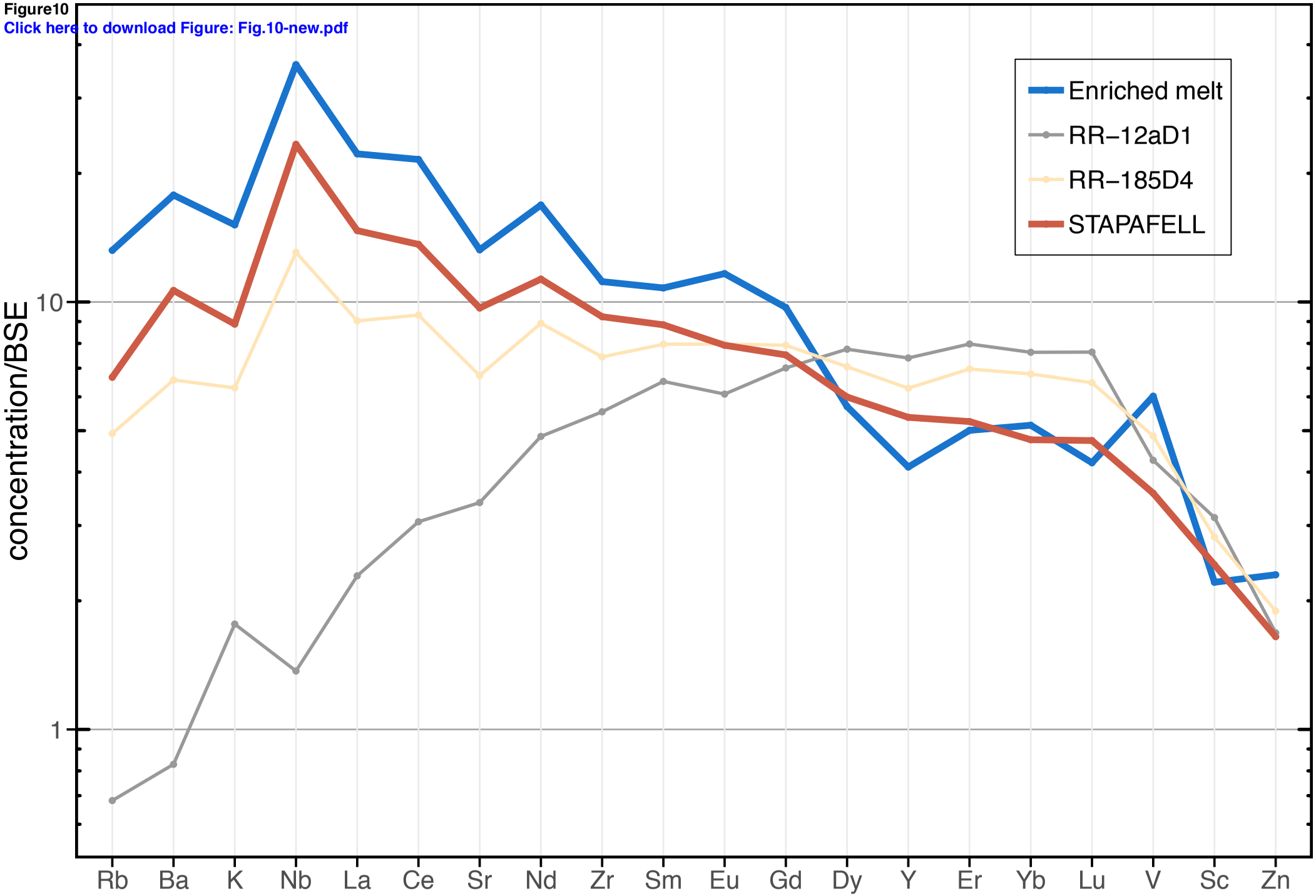

Supplementary Figure S1

Click here to download Supplementary material for online publication only: Fig.S1-new.pdf

Supplementary Figure S2

Click here to download Supplementary material for online publication only: Fig.S2-new.pdf

Supplementary Table 1

Click here to download Supplementary material for online publication only: RR-Supplementary-table-1.pdf

Supplementary Table 2

Click here to download Supplementary material for online publication only: RR-Supplementary-table-2-new.pdf

Supplementary Table 3

Click here to download Supplementary material for online publication only: RR-Supplementary-table-3.pdf

Supplementary Table 4

Click here to download Supplementary material for online publication only: RR-Supplementary-table-4-new.pdf

Supplementary Table 5

Click here to download Supplementary material for online publication only: RR-Supplementary-table-5-new.pdf